Bio-Design and Manufacturing (2021) 4:222–242
https://doi.org/10.1007/s42242-020-00122-3

RESEARCH ARTICLE

Experimental and numerical characterization of 3D-printed scaffolds under monotonic compression with the aid of micro-CT volume reconstruction

R. Baptista[1,3] · M. F. C. Pereira[2] · A. Maurício[2] · D. Rechena[3,4] · V. Infante[3] · M. Guedes[1,5]

Received: 21 October 2020 / Accepted: 15 December 2020 / Published online: 8 January 2021

Abstract

Even when damaged by injury or disease bone tissue has the remarkable ability to regenerate. When this process is limited by large size bone defects, tissue engineering is responsible for restoring, maintaining or improving tissue function. Scaffolds are support structures, designed to be implanted in the damaged site, supporting mechanical loads and protecting the regenerating bone tissue. In this paper, 3D-printed PLA scaffolds with three different porosity values and two different geometries were experimentally and numerically characterized. Micro-CT analysis showed that fused filament fabrication can be used to produce scaffolds with the desired porosity and 100% of interconnected pores. Under monotonical compression, scaffolds apparent compressive modulus increased from 89 to 918 MPa, while yield stress increased from 2.9 to 27.5 MPa as porosity decreased from 70 to 30%. Open porosity decreased up to 8% on aligned scaffolds and 14% on staggered scaffolds, after compression, while scaffold's surface-to-volume ratio highest reduction (7.48 to 4.55 mm^{-1}) was obtained with aligned low porosity scaffolds. Micro-CT volume reconstruction allowed for scaffold simplified numerical models to be built and analyzed. Excellent agreement was found when predicting scaffold's apparent compressive modulus. Overall, it can be concluded that 3D printing is a viable scaffold manufacturing technique for trabecular bone replacement.

Keywords Scaffold · Pore design · Mechanical behavior · Micro-CT analysis · Finite element method

Introduction

Bone tissue has the remarkable ability to regenerate when damaged by injury or disease, although this process can be hindered by large size bone defects. In this case, bone tissue engineering (BTE) can be used to restore or improve tissue function, namely through the use of scaffolds. Scaffolds are porous support structures, designed to be implanted on the damaged site to provide a reproducible, biocompatible, and biodegradable structure that replicates the mechanical characteristics of bone tissue, protecting it during regeneration [1]. Depending on the selected material and manufacturing technique, it is possible to develop scaffolds with structure and mechanical performance closely resembling those of bone. Scaffolds' mechanical properties should be sufficiently high to protect new bone tissue from excessive loading, including under compression. Simultaneously, scaffolds must present a fully percolated pore structure, enabling cell migration, adhesion and growth, as well as cell oxygenation and nutrition, culminating in the production of extracellular matrix (ECM) [2].

Supplementary Information The online version contains supplementary material available at (https://doi.org/10.1007/s42242-020-00122-3).

✉ R. Baptista
ricardo.baptista@estsetubal.ips.pt

1 CDP2T, Departamento de Engenharia Mecânica, Escola Superior de Tecnologia de Setúbal, Instituto Politécnico de Setúbal, 2910-761 Setúbal, Portugal

2 CERENA, DECivil, Instituto Superior Técnico, Universidade de Lisboa, Av. Rovisco Pais, 1, 1049-001 Lisbon, Portugal

3 IDMEC, Instituto Superior Técnico, Universidade de Lisboa, Av. Rovisco Pais, 1, 1049-001 Lisbon, Portugal

4 IPFN, Instituto Superior Técnico, Universidade de Lisboa, 1049-001 Lisbon, Portugal

5 CeFEMA, Instituto Superior Técnico, Universidade de Lisboa, Av. Rovisco Pais, 1, 1049-001 Lisbon, Portugal

Conventional fabrication techniques of polymeric scaffolds—e.g., solvent casting/particulate leaching [3–5], fiber bonding [6–8], and thermally induced phase separation [9–11], are limited by low reproducibility and long preparation times. In this context, alternative methods have been studied and implemented in recent years, including additive manufacturing processes. The most used is the fused filament fabrication (FFF) process (also known under the trademark Fused Deposition Modeling, FDM), where the structure is produced layer by layer using data from computer aided design (CAD) files [12]. Since it renders strict control over the shaping process, FFF makes possible to create identical macroporous scaffolds of different chemistry and microporosity [13]. Several studies have proposed the FFF production technique in different areas of scaffolds application. Namely, this technique was used to produce poly(lactic acid) (PLA) gyroid scaffolds [14], where the printing parameters were optimized by analyzing scaffold porosity (measured by micro-CT) and mechanical properties (assessed by compression test) versus the effect of geometry, printing resolution and PLA crystallinity. In another study [15], the printability of a poly(e-caprolactone)/bioactive glass (PCL/BAG) composite and L-lactide/e-caprolactone 75/25 mol% copolymer (PLA/PLC) was demonstrated; the authors also showed that the resulting compressive properties were significantly dependent on porosity level and structural geometry. A review was also presented [16] regarding the relationship between geometry and performance of BTE scaffolds produced by the FFF technique. Nevertheless, no general consensus was found yet concerning the optimal scaffold geometry for biological performance, indicating the need of further research with medical/biological focus. In this frame Roseti et al. [2] produced a variety of scaffolds to study the improvement of cell viability, attachment, proliferation and homing, osteogenic differentiation, vascularization, host integration and load bearing. Zhang et al. [17] reported a study on materials selection, scaffold design optimization and their preclinical and clinical applications in the repair of critical-sized bone defects. Both works reported encouraging results, but pointed out that the obtaining of regulatory approval requires more in-depth studies taking place at large scale [2]. They also highlighted the improvement of scaffold microstructure as a mandatory target, namely by incorporation of clinical imaging and mathematical modeling into the forming process.

From all scaffold characteristics, pore size, scaffold porosity, pore configuration (or design) and layer thickness, the first two are considered to be the most important for cell adhesion, proliferation and tissue regeneration [17]. Scaffolds must provide high porosity and a pore size between 200 and 500 µm, for optimal cell penetration, migration and growth, as well as for optimal tissue vascularization and regeneration [2]. Hollister et al. or Cavo and Scaglione, have reported the use of pores with sizes up to 1200 µm with contradictory results. While Cavo and Scaglione achieved better cell proliferation and adhesion, after 7 days of in vitro experiments, when using 600 µm pore scaffolds vs 300 and 900 µm ones [18]. Hollister et al. reported no significant differences between 300 and 1200 µm pore scaffolds regarding in vivo bone formation [19]. Although macroporosity plays an important role on osteogenic outcomes, porosity, permeability or pore surface roughness may enhance cell adhesion, proliferation and bone formation [20].

Although the literature on the experimental mechanical behavior of scaffolds is quite vast, numerical studies have not received many contributions. Moroni et al. [21] obtained a relative deviation less than 15% between the experimental and numerical results for all of the constructs with dynamic stiffness above 1 MPa. They conclude that the mathematical model introduced can be used to predict the dynamic stiffness of a porous polyethyleneoxide-terephthalate/polybutylene-terephthalate (PEOT/PBT) scaffold, and to choose the biomechanically optimal structure for tissue engineering applications. Wieding et al. [22] carried out a numerical approach to match open-pore metallic scaffold structures to the elastic properties of human cortical bone, and found that the use of a numerical optimization process is a feasible tool to reduce the amount of required titanium without negatively influencing the biomechanical performance of the scaffold.

The current paper aims to contribute to the effort of scaffolds design optimization, by developing a numerical model of 3D-printed scaffolds configuring three different porosity values and two different geometries. A detailed characterization of the scaffolds behavior under experimental mechanical testing and their geometrical and morphological characterization obtained by microtomography (micro-CT) and scanning electron microscopy (SEM) are provided and compared with results obtained by numerical simulation. The developed model is expected to reliably estimate the behavior of FFF scaffolds (within the tested geometries) with variable porosity, without the need to carry out experimental mechanical tests at the large scale required in health care.

Materials and methods

Materials

PLA material for 3D printing was acquired from BQ Engineering in the form of ∅ 1.75 mm filament. According to the manufacturer PLA filament density is 1.24 g/cm^3, with melting temperature in the 145–160 °C range and glass transition temperature between 56 and 64 °C; the recommended printing temperature range is 200–220 °C.

Scaffolds design and manufacturing

Scaffolds were manufactured by FFF using a Blocks Zero (Blocktec) 3D Printer. Two different geometries were produced by manually creating *gcode* files, that are interpreted by the 3D printer. Each layer was printed in a single motion, by depositing parallel filaments at a constant rate (30 mm/s) in alternate directions (Fig. 1a). A ∅ 400 µm nozzle was used for all printing jobs, creating a filament with approximately equal width (a). Three filament offset distances d_{offset} were used (Table 1), creating scaffolds with 30, 50 and 70% infill. In one geometry—*Ortho*, each sequential layer was rotated by 90°, creating a 0/90° orthogonal aligned grid. The scaffold main pores have square shape, with tailored sizes and areas between 171 and 933 µm and 0.029 and 0.870 mm^2 (Table 1). In the other geometry—*2xDispl*, a staggered double-layer configuration was used. Each sequential layer was repeated and, by displacing the layer origin by $d_{offset}/2$, the support points became suspended, introducing filament bending on the scaffold. In this configuration the scaffold main pores have the same dimensions as in *Ortho* counterparts, but the underlying layers are expected to reduce vertical motion of eventual cells, allowing for better cell support [16] (Fig. 1b). All scaffolds were produced with previously optimized parameters [23, 24] and dimensions complying with ASTM-D695 standard (12.7 × 12.7 × 25.4 mm). Printing temperature was set to 220 °C and layer thickness to 200 µm. Resulting scaffold lateral pores height is 200 µm (b) for the single layer configuration, and 400 µm (c) for the double-layer configuration.

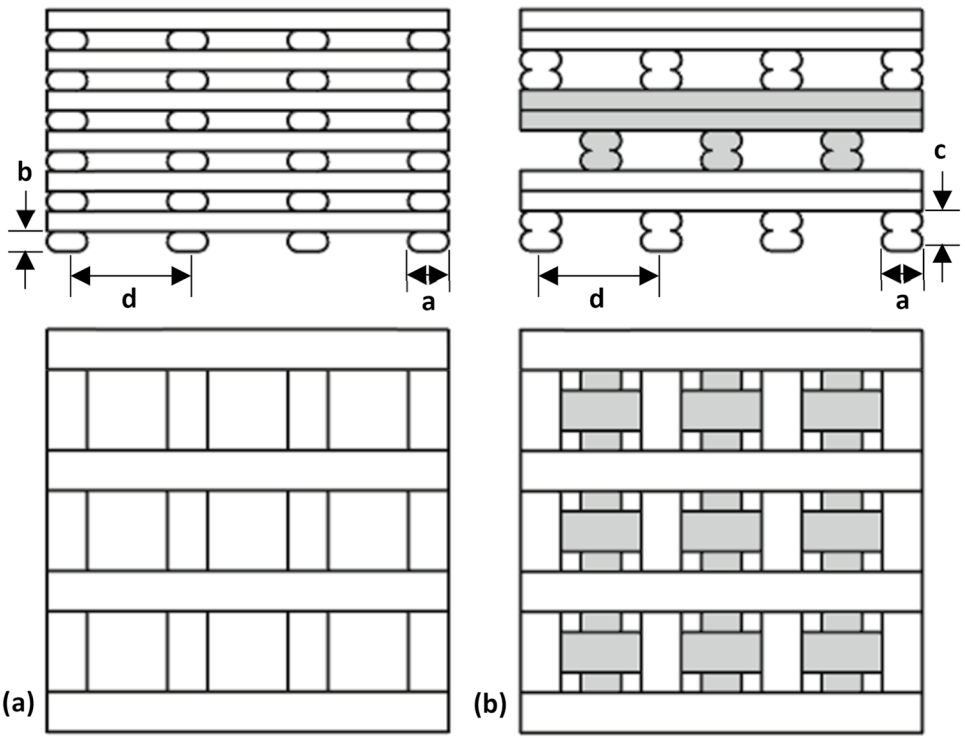

Fig. 1 Designed scaffolds front view (upper images) and top view (lower images): **a** single layered aligned (Ortho), and **b** double-layered staggered (2xDispl); $a = 400$ µm, $b = 200$ µm, $c = 2 \times 200$ µm and $d = d_{offset}$ (1333, 800 or 571 µm)

Table 1 Scaffold design parameters (infill, filament offset and staggered filament displacement), theoretical porosity and pore size and area values, and layer thickness

Specimen	Scaffold infill (%)	Filament offset (µm)	Filament displacement (µm)	Scaffold porosity (%)	Pore size (µm)	Pore area (mm^2)	Layer thickness (µm)
Ortho-30	30	1333	–	70	933	0.870	200
Ortho-50	50	800	–	50	400	0.160	
Ortho-70	70	571	–	30	171	0.029	
2xDispl-30	30	1333	666.5	70	933	0.870	2 × 200
2xDispl-50	50	800	400.0	50	400	0.160	
2xDispl-70	70	571	285.5	30	171	0.029	

Morphological analysis

Scanning electron microscopy

SEM (Hitachi S2400) was used to study the morphology, filament width, pore area and defects features of FFF-printed PLA scaffolds before and after mechanical testing. Samples were previously coated with Au–Pd alloy to assure adequate electrical conductivity during observation. Measurement of scaffolds dimensions (pore size, filament width and pore area) were carried out by image analysis using the ImageJ freeware (https://imagej.nih.gov/ij/); at least 20 random positions were measured in each sample for reproducibility assessment.

Differential scanning calorimetry

Differential Scanning Calorimetry (DSC) was carried out (TA Instruments, Q200) to evaluate the effect of FFF and of mechanical testing on the degree of crystallinity of the used PLA polymer. Samples of as-supplied filament, samples removed from scaffolds after FFF and samples removed from scaffolds compressed up to 40% strain were encapsulated in aluminum pans and heated up to 230 °C at 15 °C/min heating rate, under nitrogen gas flow (20 ml/min). At least three samples (approx. 9 mg), were tested for each condition to ensure reproducibility. The enthalpy value associated with cold crystallization and melting events was measured as the area under the corresponding peak in the DSC plot. The degree of crystallinity associated with cold crystallization (X_{cc}) and to the semi-crystalline PLA polymer (X_{pol}) were, respectively, calculated using Eqs. 1 and 2 [25–27].

$$X_{cc} = 100 \times \frac{\Delta H_{cc}}{\Delta H_m^0} \tag{1}$$

$$X_{pol} = 100 \times \frac{\Delta H_m - \Delta H_{cc}}{\Delta H_m^0} \tag{2}$$

where ΔH_m and ΔH_{cc} are, respectively, the enthalpy of melting and the enthalpy of cold crystallization (which takes place during the measurement); ΔH_m^0 is the enthalpy of melting for a pure PLA crystal of infinite size (93.7 J/g) [28].

Micro-CT

X-ray micro-computed tomography (micro-CT) was used to assess the three-dimensional structure of as-printed and deformed scaffolds. Digital radiographs were acquired with a micro-CT scanner (Bruker, SkyScan 1172), by rotating the specimen over 180° with a fixed 0.5° step. Experimental conditions were set to optimized acquisition time and best image contrast, with pixel size resolution of 18.09 µm and an average of five radiographs per position. Slice reconstruction was carried out with NRecon®1.6.3 routine, and volumetric visualization was achieved with DataView® and CTvox® programs (https://www.bruker.com). Volume analysis was carried out afterward using CT-Analyser software (https://www.bruker.com). Digital Imaging and Communications in Medicine (DICOM) formatted images were loaded and the region of interest (ROI) was defined, using polygons to interpolate the scaffold shape (including PLA material and pore geometry) along its full height. An attenuation coefficient filter was set between 0.00252 and 0.01604 to create a binary image set, which was further copied to the custom processing module, for ROI despeckle and complete 3D analysis. Total ROI (V_T) and object (V_O) volume, were used to calculate scaffold density (ρ) and porosity (P) (Eq. 3).

$$P = 100(1 - \rho) = 100\left(1 - \frac{V_T}{V_O}\right) \tag{3}$$

Scaffolds open porosity P_{open} (where closed or not interconnected pores are not taken into account) was also calculated; P_{open} is expected to match the tailored 70, 50 and 30% design values, in order for all pores to be interconnected. Object surface area (S) was determined, enabling calculation both of scaffolds surface-to-volume ratio S_O (Eq. 4) and surface density S_ρ (Eq. 5)

$$S_O = \frac{S}{V_O} \tag{4}$$

$$S_\rho = \frac{S}{V_T} \tag{5}$$

All measures were carried out in as-printed and deformed scaffolds after 40% compression, to assess the effect of mechanical deformation upon pore collapse and surface density variation.

Mechanical testing

Scaffolds were experimentally tested under monotonical compression. An electromechanical test machine (TS300, Impact Test Equipment), with a 50 kN load cell, was used to carry out mechanical compression with a constant 1 mm/min speed until strain ε reached 40%. Scaffold´s apparent compressive yield stress σ and compressive modulus E were estimated for each specimen.

Compression simulation by finite element method

Although scaffold filaments were tailored for constant width (400 µm) and height (200 µm) (Fig. 2a), local variations (Fig. 2b) are to be expected as a consequence of stretching due to filament suspension and high printing speed [29]. In

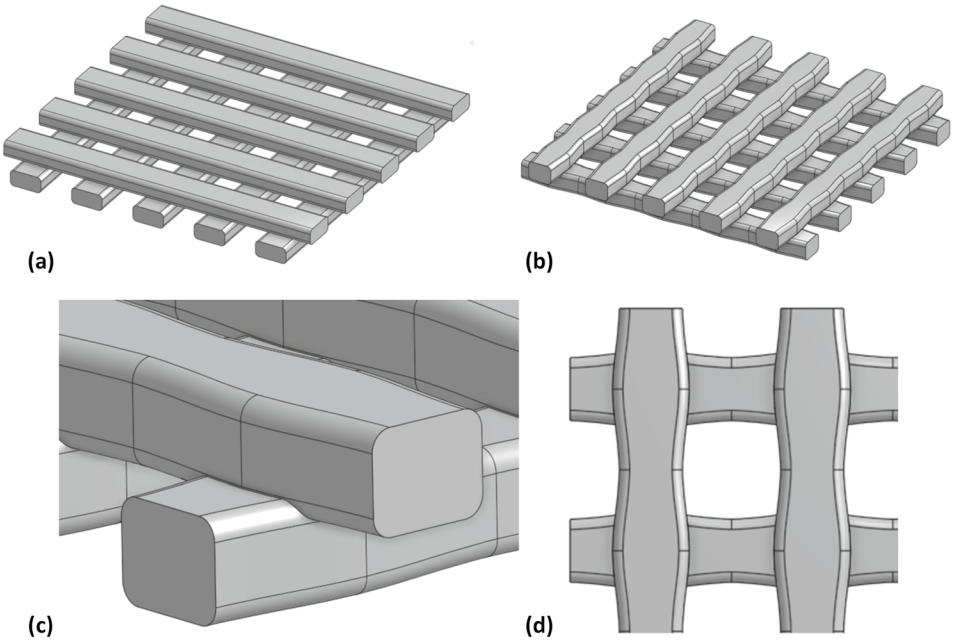

Fig. 2 **a** Tailored single layer scaffold with constant filament width ($a = 400$ µm) and thickness ($b = 200$ µm), **b** simulated single layer scaffold with different minimum (a_{min}) and maximum (a_{max}) filament width due filament stretching, representing **c** interference with previously printed layers, **d** resulting pore shape

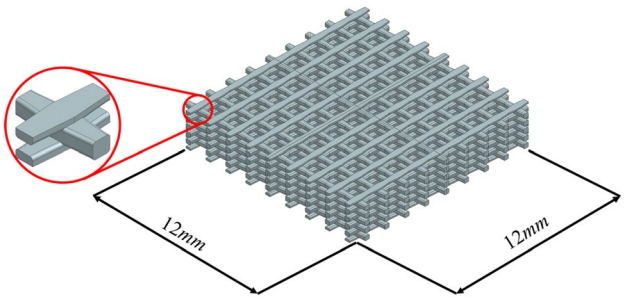

Fig. 3 Generation of a scaffold CAD model from a periodic volume

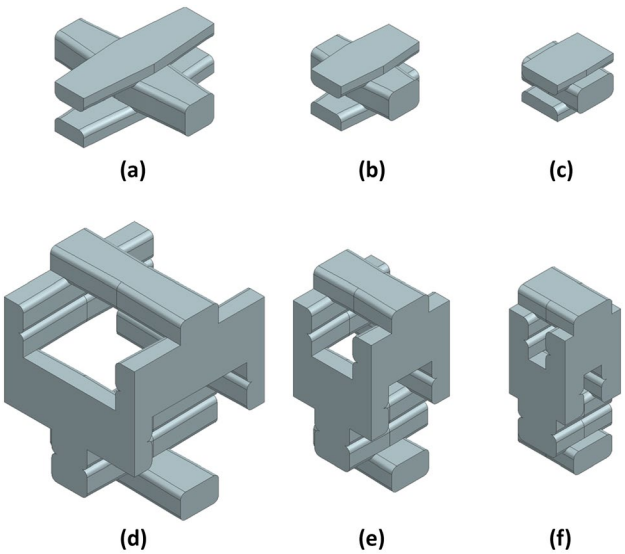

Fig. 4 Repeating structure of each simulated scaffold **a** Ortho-30, **b** Ortho-50, **c** Ortho-70, **d** 2xDispl-30, **e** 2xDispl-50, **f** 2xDispl-70

as much, for each scaffold configuration a simplified finite element method (FEM) model was produced using the results of micro-CT volume reconstruction regarding minimum (a_{min}) and maximum (a_{max}) filament width distribution (Sect. 3.2).

The CAD model for each scaffold was built through the patterning of periodic structures over two orthogonal directions so that a 12 mm × 12 mm cross section area was obtained. The resulting geometry was then patterned on the direction perpendicular to the cross section in order to obtain 5 cross section instances along its perpendicular direction (Fig. 3). Six different CAD models were generated from the periodic structures as presented in Fig. 4.

FEM models were constructed in the NX Nastran's linear elastic solver SOL101, using CTETRA(4) linear elements. Element size was set to 0.125 mm for all scaffold configurations, except for 2xDispl-70 where, due to complex model geometry, element size was set to 0.09375 mm.

A convergence study demonstrated that using smaller element sizes, did not affect the obtained stress and strain fields. A normal strain field, ε, of 0.01 was enforced on the top and bottom of the scaffold model and symmetry boundary conditions were enforced on its midplanes folds. The reaction force was then computed at one of the scaffold boundaries. The apparent compressive modulus for each scaffold E_{num} was then determined using Eq. 6, where F is the total reaction at one of the boundaries and A is the model cross-sectional area [30].

$$E_{num} = \frac{F/A}{\varepsilon} \tag{6}$$

Numerical results were afterward compared with the corresponding experimental values, and the relative error for each scaffold geometry was computed. Since the apparent compressive moduli were computed through linear elastic FEM models, the obtained moduli are proportional to the Young's modulus of the filaments E_{fill}. In order to determine the optimal E_{fill} value that should be applied to the model, a calibration between numerical and experimental apparent compressive modulus was performed. Filament Young's modulus was estimated by minimizing the average error between all scaffold models (Eq. 7):

$$\min_{E_{fill}} \frac{1}{6} \sum_{i=1}^{6} \left| \frac{E_{num} - E_{exp}}{E_{exp}} \right|_i \tag{7}$$

Results

Geometrical characterization

Low magnification images of printed scaffolds are shown in Fig. 5. Single-layer aligned scaffolds (Ortho, Fig. 5a–c) clearly display not constant printed filament width, contrarily to design impositions (Fig. 1a, b). This is expected to result from filament stretching during extrusion, which leads to smaller width values as distance from crossover points (which act as support sites) increases [31]. Table 2 shows a minimum value of 299 ± 18 μm and a maximum of 403 ± 23 μm for the *Ortho-30* scaffold. As scaffold infill increases to 50 (Fig. 5b) and 70% (Fig. 5c) the difference between the maximum and minimum obtained values decreases (Table 2), reaching the lowest difference (36 μm) for the *Ortho-70* scaffold. This is expected to result from the concomitant decrease in offset distance between filaments, minimizing the polymer stretching effect. Low (Fig. 5d–f) and high magnification images (Fig. 6b) show different behavior for double-layer staggered scaffolds (*2xDispl*). The described stretching effect is visible for the "first" layer, but

Table 2 Filament minimum, maximum and average width, and pore area in single-layer aligned and double-layer staggered scaffolds as measured by SEM image analysis

Specimen	a_{min} (μm)	a_{max} (μm)	a_{med} (μm)	Pore area (mm^2)
Ortho-30	299 ± 18	403 ± 23	344 ± 56	1.007 ± 0.027
Ortho-50	318 ± 11	378 ± 16	344 ± 34	0.188 ± 0.003
Ortho-70	351 ± 11	387 ± 4	369 ± 21	0.045 ± 0.005
2xDispl-30	372 ± 5	390 ± 11	383 ± 16	0.903 ± 0.011
2xDispl-50	375 ± 7	380 ± 15	377 ± 55	0.173 ± 0.015
2xDispl-70	382 ± 6	391 ± 6	386 ± 7	0.034 ± 0.002

a_{min}: minimum filament width; a_{max}: maximum filament width; a_{med}: average filament width

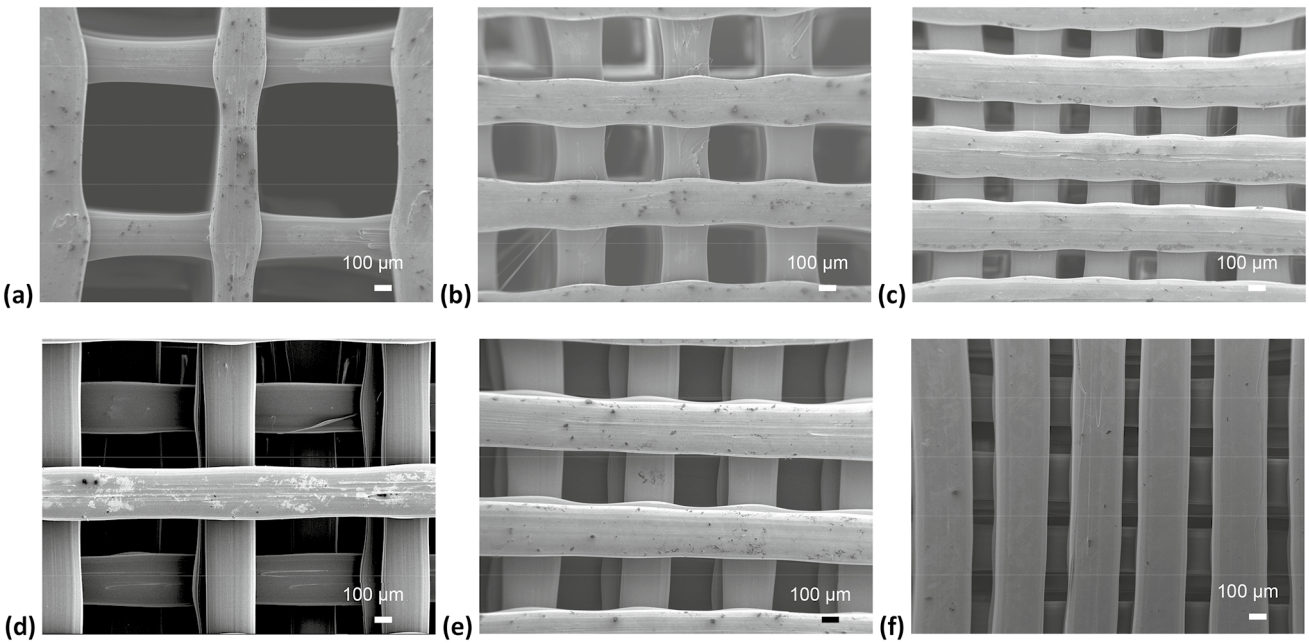

Fig. 5 Top view low magnification SEM images of filament stretching with different a_{max} and a_{min} in **a** Ortho-30, **b** Ortho-50 and **c** Ortho-70 scaffolds; scaffolds with bottom staggered layers, expected to offer restricted vertical cell movement in **d** 2xDispl-30, **e** 2xDislp-50 and **f** 2xDispl-70 scaffolds

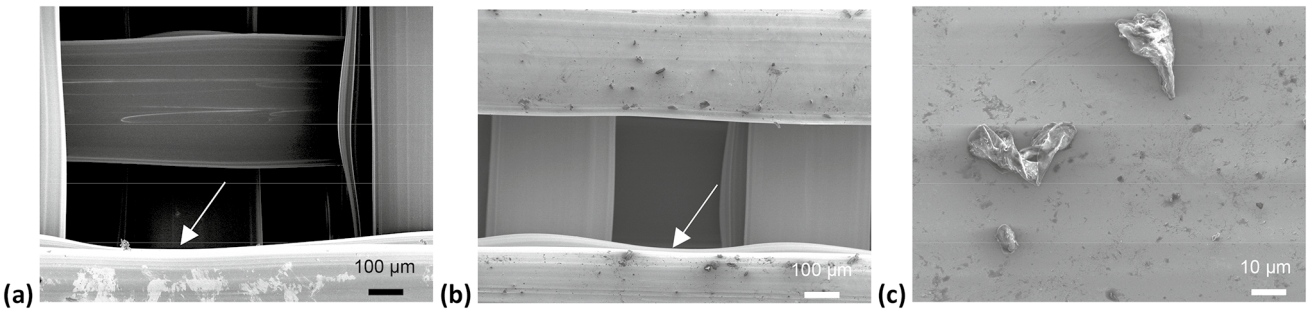

Fig. 6 Detail of bottom staggered layer in **a** 2xDispl-30 and **b** 2xDispl-50 scaffolds (top view), showing minimized stretching on the second printed layer (arrows point to higher stretching on the first layer); **c** Defects on the surface of Ortho-30 filaments (top view), detail of small particles on the surface

polymer stretching is minimized in the subsequent layer. When printing a double-layer configuration, the second layer is printed with full support, over the first layer that has meanwhile cooled down. The difference between maximum and minimum filament width is thus smaller in this configuration, reaching a minimum value of 9 µm (*2xDispl-70*). The presence of staggered layers, while not affecting pore shape or dimensions (Fig. 6a), adds additional restriction to the vertical motion of incorporated cells, increasing the probability of cell adhesion and growth [16, 17]. Filament width is still proportional to scaffold infill, with minimum filament width increasing from 372 ± 5 µm (*2xDispl-30*) to 382 ± 6 µm (*2xDispl-70*). Overall, filament width is higher in double layer than in single-layer scaffolds, but always smaller than the nozzle's diameter (400 µm). It should be mentioned that in all scaffolds the filament surface was covered with small particles (Fig. 6b, c), which have been attributed to 3D printing process defects, with potential to positively influence cell adhesion and growth [1, 32].

Pore size is highly dependent on scaffold infill. As would be expected, pore area decreases with increasing scaffold infill (Table 2), for both single-layer aligned and double-layer staggered scaffolds. Maximum pore area was obtained for *Ortho-30* scaffold (1.007 ± 0.027 mm^2), while minimum scaffold pore area was obtained for *2xDispl-70* scaffold (0.034 ± 0.002 mm^2). Pore area is a function of scaffolds' filament width [33], increasing as filament width decreases. Since filament width was lower for single-layer scaffolds, pore area was higher when compared to that of pores in double-layer scaffolds. Finally, pore area values are higher than the corresponding design values in all produced scaffolds (Table 1), while minimum filament width showed opposite behavior. Again, the deviation between measured and designed pore fraction is higher in single-layer aligned scaffolds than in double-layer staggered scaffolds and substantially decreases with increasing infill.

Mechanical behavior

All scaffold configurations were tested under monotonic compression conditions. Figure 7 shows the obtained stress–strain relations for single-layer aligned scaffolds (Fig. 5a–c) and for double-layer staggered scaffolds (Fig. 5d–f). On both configurations, the shape of the stress–strain curve does not totally comply with the typical curve for porous polymeric materials. The typical curve comprises three different regions: the initial linear region, corresponding to the linear deformation of the porous

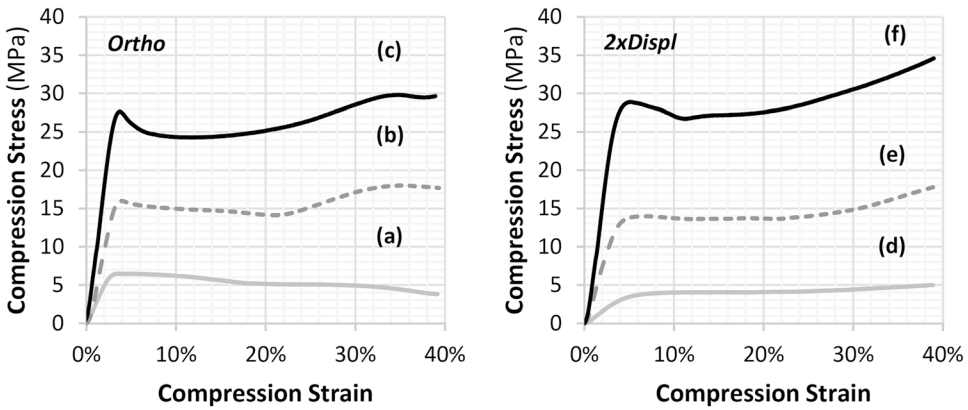

Fig. 7 Stress–Strain compression curves for single-layered aligned scaffolds with **a** 30% (Ortho-30), **b** 50% (Ortho-50) and **c** 70% (Ortho-70) infill; and double-layered staggered scaffolds with **d** 30% (2xDispl-30), **e** 50% (2xDispl-50) and **f** 70% (2xDispl-70) infill

structure; a constant stress plateau follows, associated with the progressive collapse of pores wall structure, leading to structural damage accumulation; and finally the total collapse of the remaining open pores, leads to a very rigid structure, resulting in a region of exponential stress increase [34, 35]. Only the first two regions are clearly identifiable in the produced scaffolds under the used test conditions.

Yield stress occurs around 4% strain for both aligned and staggered scaffolds, while both yield stress and apparent compressive modulus increases with scaffold infill (Table 3). In aligned scaffolds (Fig. 7a–c) yield stress values range from 6.4 to 27.5 MPa and apparent compressive modulus values range from 239 to 918 MPa when infill increases from 30 to 70%. In staggered scaffolds (Fig. 7d–f) yield stress values range from 2.9 to 27.5 MPa and apparent compressive modulus varies between 89 and 913 MPa. These values indicate that, as expected, both yield stress and apparent compressive modulus of staggered scaffolds are affected by structural bending. In the *2xDispl-30* the apparent compressive modulus of 89 MPa corresponds to a 63% decrease compared to its aligned scaffold counterpart. Increasing scaffolds infill to 50% reduces that difference to 23%, while almost no difference was found between aligned and staggered scaffolds with the highest tested infill (70%). This indicates that increasing scaffolds infill (i.e., decreasing structural porosity), minimizes structural bending, leading to increased rigidity.

Regarding the third stress–strain region, stress values increase appears not to reach exponential growth in scaffolds with 50 and 70% infill, both in the case of single-layered aligned (Fig. 7b, c) and of double-layered staggered (Fig. 7d–f) configurations. This indicates that the maximum applied compression strain (40%) is not enough to cause full macropores collapse. In single-layered aligned scaffolds with 30% infill, stress decreases in the third region (Fig. 7a), while it appears to remain constant throughout in double-layered staggered scaffolds with 30% infill (Fig. 5d). SEM observation after monotonic compression test showed that scaffolds with 50 and 70% infill suffer extensive overall deformation (e.g., Fig. 8a), but individual filaments remain wholesome. However, scaffolds with 30% infill display numerous fractured filaments. Interestingly, fracture appears to occur in brittle mode in

Table 3 Single-layer aligned and double-layer staggered scaffolds apparent compressive modulus and yield stress

Specimen	E_{exp} (MPa)	σ_y (MPa)
Ortho-30	239 ± 31	6.4 ± 0.6
Ortho-50	570 ± 19	16.0 ± 0.3
Ortho-70	918 ± 22	27.5 ± 0.4
2xDispl-30	89 ± 3	2.9 ± 0.1
2xDispl-50	414 ± 5	12.9 ± 0.3
2xDispl-70	913 ± 5	27.5 ± 0.1

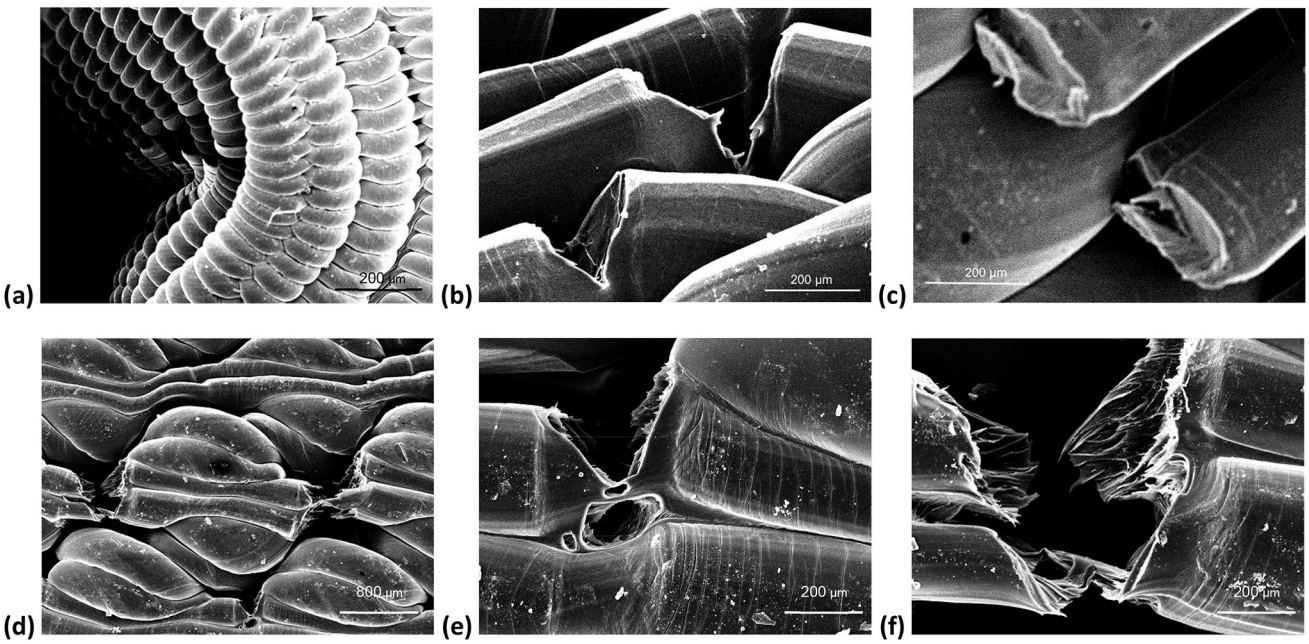

Fig. 8 Low magnification SEM images after monotonic compression test. **a** Example of extensive structural deformation (Ortho-50, front view). Brittle fracture in Ortho-30: **b** crack opening, and **c** fracture surface. Ductile fracture in Disp-30: **d** general front view; **e** crazing and pore coalescence; and **f** fracture surface

the case of aligned scaffolds (Fig. 8b, c) and in ductile mode in staggered scaffolds (Fig. 8d–f).

Since mechanical properties of polymers are significantly influenced by their degree of crystallization [23, 36], DSC thermal analysis was used to assess the effect of FFF manufacturing and of compression testing upon the crystallinity of the used PLA material. Crystallinity fraction was calculated from the enthalpy values associated with polymer cold crystallization (Eq. 1) and melting (Eq. 2).

All obtained DSC heating plots (Fig. 9a, b) show two endothermic peaks corresponding to glass transition and to crystal melting, and one exothermic peak corresponding to cold crystallization. Cold crystallization corresponds to the ability of unstable chains (whose presence in the material results from chain rearrangement being hindered by fast cooling) to go through posterior crystallization, with formation of new ordered structures at the transition zone between existing crystallites and amorphous regions [27]. The tested samples (including as-supplied filament, printed scaffolds and scaffolds after compression test) displayed glass transition onset within 69.2 ± 1.1 °C; cold crystallization took place approx. in the 99–122 °C range; melting onset occurred around 135 °C, and was finished below 160 °C (well below the used FFF temperature, 220 °C) (Fig. 9a, b). These values are in good agreement with literature reports for semi-crystalline PLA [26, 37–39]. It should be mentioned that cold crystallization is present in polymers prone to crystallize but in which crystallization is (partially) prevented by fast cooling from the melt state, such as PLA [26]. In the course of DSC analysis, the mobility of the macromolecular chains is severely restricted while test temperature is below T_g. However, above that temperature

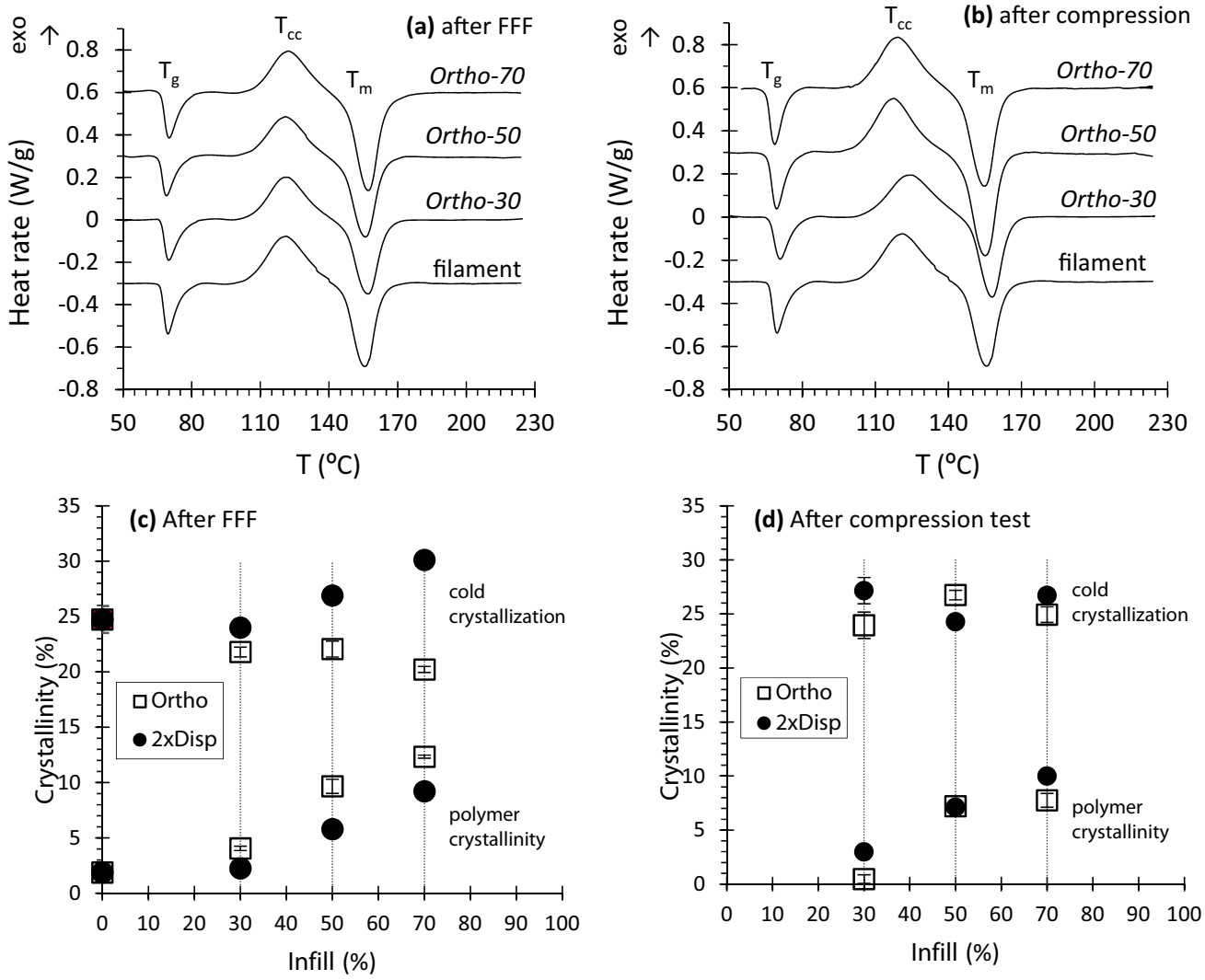

Fig. 9 Thermal analysis results. DSC plots obtained on heating up to 230 °C for aligned scaffolds **a** before, and **b** after compression test. Evolution of calculated PLA crystallinity values with manufacturing and testing demands on **c** aligned, and **d** staggered scaffolds

small crystallites are allowed to form, and the ability of PLA to rearrange manifests [27]. In as much, the microstructural history of the produced PLA scaffolds can be approached through the enthalpy values associated with the thermal phenomena developed in the course of DSC heating: while the DSC plot and transition temperatures of the PLA material after withstanding FFF at 220 °C (e.g., Fig. 9a, b) are similar to as-supplied material, significantly different values of enthalpy associated with cold crystallization and melting thermal phenomena arise (Fig. 9c, d).

A crystallinity fraction around 2% was calculated for the used PLA filament, while the corresponding cold crystallization amounted to approx. 24%. This indicates that filament cooling after forming was fast enough to avoid PLA chain rearrangement [26] resulting in a mainly amorphous material [26, 27], that has however the potential to further crystallize. The FFF process has the ability to prompt PLA's ability to rearrange and after printing PLA not only presents higher crystallinity than in the filament form, but also displays increasing crystallinity with increasing scaffold infill. This is expected to result from the higher number of stretching operations and higher residence time at melt temperature required to fulfill the scaffolds design, introducing increased chain mobility and chain alignment in the course of the FFF extrusion operation [26]. For the same reason the degree of crystallinity is higher in single-layer aligned scaffolds (χ_{pol} ranging between approx. 4 and 12% for infill between 30 and 70%, Fig. 9c) than in double-layer staggered scaffolds (χ_{pol} between 2 and 9% for infill between 30 and 70%, Fig. 9d).

Aligned scaffolds present similar cold crystallization values after AM regardless of the infill ($\chi_{cc} = 21.9 \pm 1.0$), and somewhat lower (8.8%) than as-supplied filament. In staggered scaffolds the amount of cold crystallization increases around 13% compared to as-supplied filament (possibly because of higher cooling rate) and is similar for all infills ($\chi_{cc} = 27.0 \pm 3.1$) expectedly because of their similar thermal history. After compression test PLA crystallinity decreases for aligned scaffolds (χ_{pol} ranging between approx. 0.5 and 7.8% for infill between 30 and 70%, Fig. 9c), while it remains approx. the same in staggered scaffolds. Also, cold crystallization after testing in aligned scaffolds increases to $\chi_{cc} = 24.9 \pm 0.9\%$ (13.4% increase), while it more slightly decreases (3.5%) in staggered scaffolds ($\chi_{cc} = 26.0 \pm 1.5\%$).

Volume analysis

Micro-CT images of as-printed aligned scaffolds are shown in Fig. 10. Apparently, filaments are evenly aligned and regularly spaced (Fig. 10, upper images) for all infill values. Top views (Fig. 10, bottom images) show crossover points where higher filament width is visible. All pores appear to be interconnected. Measured porosity values (Table 4) of as-printed scaffolds were, respectively, 2.30 and 0.80% lower and 2.66% higher than the design values of 70 (*Ortho-30*),

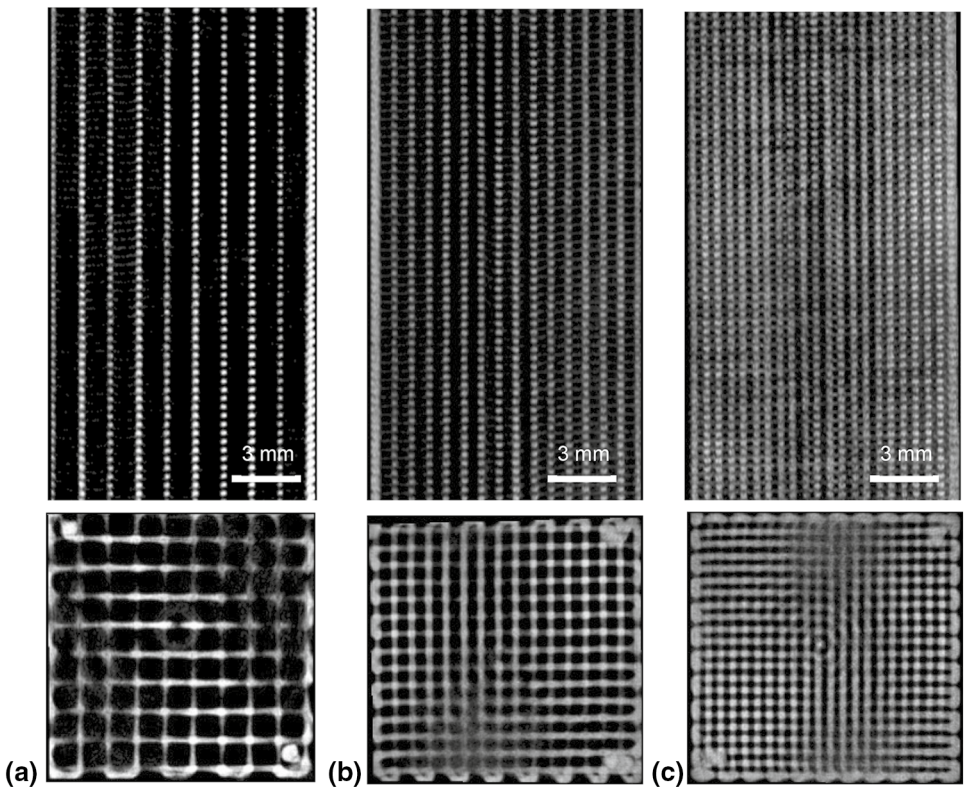

Fig. 10 Micro-CT images of single-layer aligned scaffolds. Front view (upper images) and top view (bottom images) of scaffolds with **a** 30, **b** 50 and **c** 70% infill (as-printed scaffolds)

Table 4 Micro-CT volume analysis on single-layer aligned scaffolds, before and after 40% compression testing

	Ortho-30	*Ortho-50*	*Ortho-70*
As printed			
Total porosity (%)	67.70	49.20	32.66
Open porosity (%)	67.70	49.16	32.56
Surface-to-volume ratio (mm^{-1})	9.38	8.42	7.48
Surface density (mm^{-1})	3.03	4.28	5.03
As tested			
Total porosity (%)	62.15	43.45	24.90
Open porosity (%)	62.15	43.45	24.85
Surface-to-volume ratio (mm^{-1})	7.81	6.24	4.55
Surface density (mm^{-1})	2.96	3.53	3.42

50 (*Ortho-50*) and 30% (*Ortho-70*); the best correlation was thus obtained for *Ortho-50*. Very high pore interconnectivity was achieved, with calculated closed pores fraction of only 0.1, 0.04 and 0% for 70, 50 and 30% designed scaffold infill. Object surface-to-volume ratio (an important morphological parameter, since high surface-to-volume ratio values have shown positive effects on cell adhesion and growth [30, 40]) appears to be proportional to scaffold porosity, decreasing from 9.38 to 7.48 mm^{-1} as porosity decreases from 67.70 to 32.66%. The reduction in filament offset distance associated with the decrease in scaffold porosity increases the number of crossover points, thus reducing the available area for cell adhesion and growth (by a total of 0.32 mm^2). Also, decreasing scaffold filaments offset distance increases the number of filaments per layer, thus increasing the overall surface area for cell adhesion and growth. Table 4 shows that overall surface density increased as scaffold porosity decreased; surface density reached 5.03 mm^{-1} on *Ortho-70* scaffolds.

As would be expected, compression loading resulted in the deformation of the aligned scaffolds (Fig. 11). Strained structures display regions where normal deformation is present and regions where shear deformation dominates. While normal deformations lead to pore collapse and apparent compressive modulus increase, shear deformation is expected to lead to scaffold damage and failure. Isometric images and videos for all scaffold configuration are provided as supplementary materials. In fact, shear deformation acts upon filaments (Fig. 8a), originating the formation of wrinkles and folds that act as sites for microcrack initiation (Fig. 8b) and propagation [41], leading to filament brittle fracture (Fig. 8c) as previously discussed.

After compression scaffolds showed an overall porosity decrease, corresponding to reduction around 5.55, 5.75 and 7.76% for *Ortho-30*, *Ortho-50* and *Ortho-70* scaffolds (Table 4). The porosity decrease is expected to result mainly from the compression of macropores in the constant stress region of the stress–strain curve (Fig. 5), with significant reduction in open porosity. Closed porosity also appears to have been eliminated in *Ortho-50* scaffold, and significantly decreased in *Ortho-70* scaffold. Compression additionally results in the decrease in scaffolds surface-to-volume ratio and surface density. After 40% compression strain scaffolds surface-to-volume ratio decreased around 17% for the lower infill scaffolds (*Ortho-30*) and around 39% for the higher infill scaffolds (*Ortho-70*). Similar behavior was found for surface density values. This suggests that the surface of lower porosity scaffolds is more affected by compression, since open pores collapse and filament merging toil to reduce scaffolds surface in a higher extent. It is thus to be expected that the ability for cell adhesion and growth [30, 40] will be more sensitive to scaffold deformation in scaffolds with initially lower pore volume fraction.

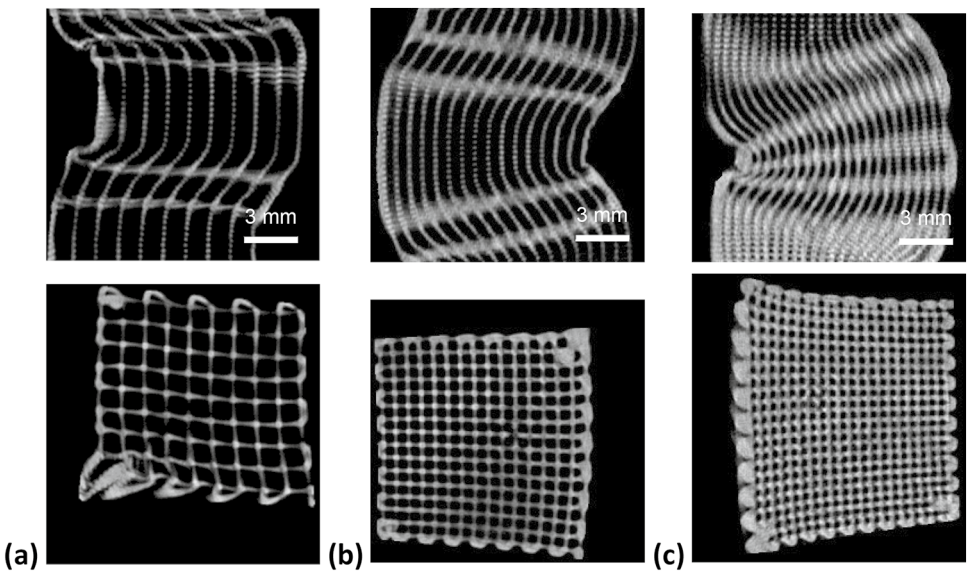

Fig. 11 Micro-CT images of single-layer aligned scaffolds after compression test. Front view (upper images) and top view (bottom images) of scaffolds with **a** 30, **b** 50 and **c** 70% infill

Micro-CT images of as-printed double-layer staggered scaffolds (Fig. 12, upper views) show the staggered layers, with filament offset creating a suspended beam. As would be expected, the number of crossover points increases as scaffold infill percentage increases. Measured porosity values (Table 5) of as-printed scaffolds were, respectively, 1.85 and 0.68% lower and 3.89% higher than the design values of 70 (*2xDispl-30*), 30 (*2xDispl-70*) and 50% (*2xDispl-50*); the best correlation was thus obtained for *2xDispl-70* scaffold. Very high pore interconnectivity was achieved, with calculated closed pores fraction of only 0.1, 0.04 and 0% for 30, 50 and 70% designed scaffold infill.

After compression, *2xDispl-30* scaffolds (Fig. 13a) display dominant normal deformation behavior, while both *2xDispl-50* (Fig. 13b) and *2xDispl-70* (Fig. 13c) scaffolds show areas where shear deformation behavior is dominant. This behavior is also visible in 3D micro-CT images provided as supplementary materials.

After compressions scaffolds porosity decreased around 22.53% for *2xDispl-30* and 13.29% *2xDispl-50* scaffolds. By staggering layers and introducing structural bending, staggered scaffold pores are more easily collapsible. Still, comparing both scaffold density and open porosity percentages, it is possible to verify the low level of closed pores. With a total of 0.1% of closed pores after 40% compression, 3D printing allows to manufacture scaffolds with almost 100% pore interconnectivity. Table 5 also shows that *2xDispl-70* scaffold was the most resistant to pore collapse. With as much as 28.09% of open pores, this scaffold outperformed the aligned counterpart. With similar apparent compressive modulus (Table 3) this behavior was to be expected.

Table 5 shows that both staggered scaffolds object surface-to-volume ratio and object surface density were inferior to those determined for their aligned counterparts (Table 4). When using a double-layer design two filament share a

Table 5 Micro-CT volume analysis on double-layer staggered scaffolds, before and after 40% compression testing

	2xDispl-30	*2xDispl-50*	*2xDispl-70*
As printed			
Total porosity (%)	68.15	53.89	29.32
Open porosity (%)	68.15	53.89	29.31
Surface density (mm^{-1})	2.88	3.99	4.77
Surface-to-volume ratio (mm^{-1})	9.05	8.66	6.76
As tested			
Total porosity (%)	54.38	40.60	28.16
Open porosity (%)	54.38	40.59	28.09
Surface density (mm^{-1})	4.02	4.23	4.81
Surface-to-volume ratio (mm^{-1})	8.81	7.12	6.70

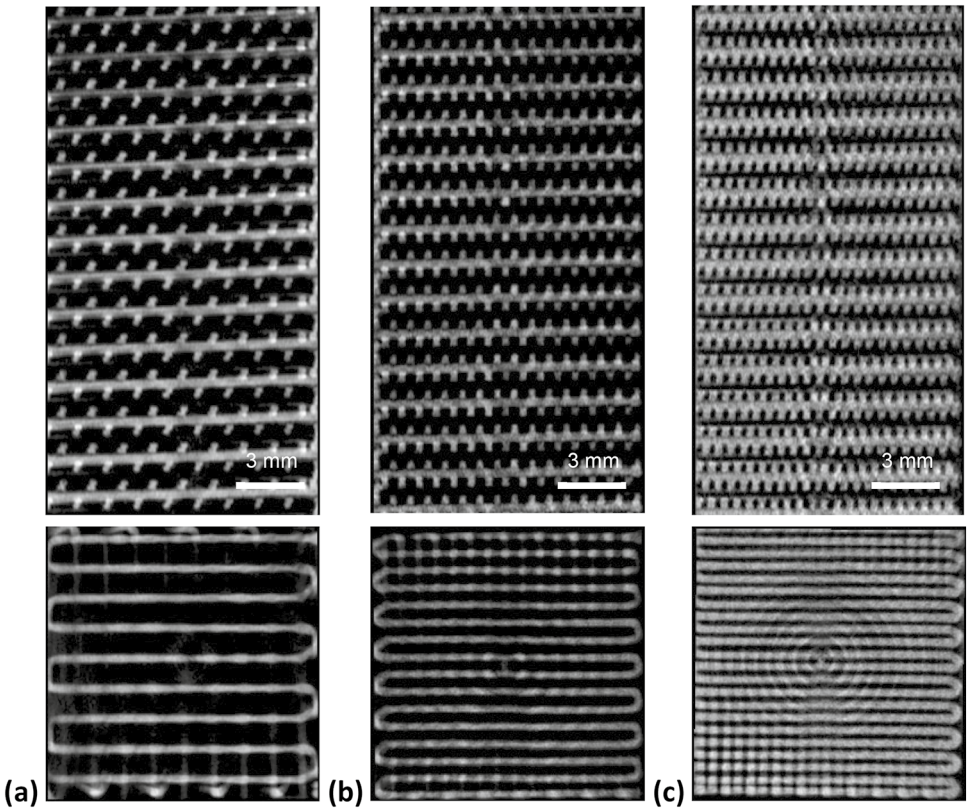

Fig. 12 Micro-CT images of double-layer staggered scaffolds. Front view (upper images) and top view (bottom images) of scaffolds with **a** 30, **b** 50 and **c** 70% infill (as-printed scaffolds)

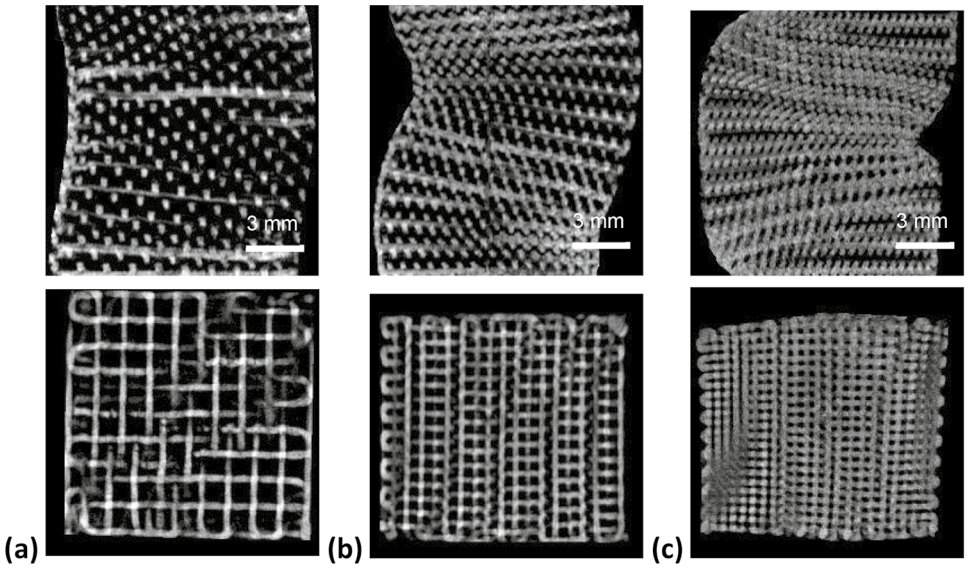

Fig. 13 Micro-CT images of double-layer staggered aligned scaffolds after compression test. Front view (upper images) and top view (bottom images) of scaffolds with **a** 30, **b** 50 and **c** 70% infill

Table 6 Filament minimum width, thickness and cross-sectional area, measured in Micro-CT analysis, for single-layer aligned and double-layer staggered scaffolds

Specimen	a_{min} (μm)	b (μm)	Cross-sectional area (mm^2)
Ortho-30	297 ± 30	268 ± 33	0.080
Ortho-50	311 ± 20	246 ± 16	0.077
Ortho-70	365 ± 31	210 ± 16	0.077
2xDispl-30	362 ± 25	492 ± 20	0.178
2xDispl-50	358 ± 05	450 ± 20	0.161
2xDispl-70	393 ± 23	405 ± 14	0.159

a_{min}: minimum filament width; b: filament thickness

common face, the final surface area available for cell adhesion is reduced. While double-layer scaffolds 3D printing improves mechanical performance [24], one should consider this side effect. Still, once compressed staggered scaffolds, both ratios showed an inferior reduction. Using a double-layer staggered configuration resulted in an increased object surface, where cells are able to growth.

Micro-CT volume analysis was also used to determine scaffold filament width and height. Table 6 shows the obtained results for both single-layer aligned and double-layer staggered scaffolds. Filament width corresponds only to the minimum obtained value (due to filament stretching under suspension). Aligned scaffolds minimum value was obtained for the *Ortho-30* scaffold (297 ± 30 μm), due to a higher distance between support points (1333 μm). And a maximum value of 365 ± 31 μm (*Ortho-70*), where the inferior filament offset distance (571 μm) reduces stretching to a minimum. As mentioned, when using a double-layered configuration (Table 6) the second layer will be fully supported while printing; therefore filament width increased between 8 and 22% and is now closer to the 400 μm design value. Filament height behavior was opposite, with height decreasing with infill percentage increase. FFF 3D printing sets the amount of material to be extruded and synchronizes this value with the printing speed. Therefore, as filament width decreases, filament height must increase in order to keep filament cross-sectional area constant. Table 6 shows that Micro-CT estimated width and height correspond to cross-sectional areas very close to the design values (0.080 and 0.160 mm^2 for both single- and double-layer scaffolds, respectively).

Finite element analysis

SEM (Table 2) and micro-CT (Table 6) analysis show that filament width is not constant. As FFF 3D printing material extrusion output is constant, filament width decrease, leads to filament height increase. Material interference on crossover points (Fig. 2c), increases local filament width to a maximum value [42]. Figure 2d shows the CAD model used for FEM analysis, where filament width decreases with between crossover points. Gleadall et al. [42] consider essential to model variable filament width over crossover points, in order to capture the correct scaffolds behavior. Filament offset distances were considered equal to the designed values (Table 1) and both double-layer and staggered designs were modeled.

Filament's Young's modulus E_{fill} were estimated by minimizing the average error between the numerical and experimental results. An E_{fill} of 1903 MPa was obtained with an average error of 6.93×10^{-9}%. Table 7 presents the corrected numerical scaffold apparent compressive moduli. The lowest apparent compressive modulus occurred for the double-layered staggered scaffold and an infill of 30% whilst the highest value occurred for both scaffolds with a 70% infill. Note that, the highest experimental apparent compressive modulus occurred for the *Ortho-70* scaffold while the highest numerical modulus was obtained for the *2xDispl-70* scaffold. The *Ortho-70* scaffold did present a higher stiffness variability (±22 MPa), than the *2xDispl-70* scaffold (±5), which accounts for the difference between results.

Discussion

In this paper, a commercial FFF 3D printer was used to manufacture PLA scaffolds for trabecular bone replacement. Two different scaffold pore designs with three different pore sizes were tested under monotonic compression. Both SEM and Micro-CT analysis were performed on all specimen's configuration before testing, and Micro-CT volume analysis was also performed after 40% compression testing. Pore design and dimension influence on scaffold's mechanical performance, morphology, porosity, pore interconnectivity and object surface density was assessed. Thermal analysis was performed in order to assess the crystallinity degree on both as-printed and deformed PLA scaffold material. Crystalline and amorphous polymers may show brittle to ductile fracture behavior, therefore DCS thermal analysis provided good correlation with the resulting scaffold fracture mode. Numerical simulation allowed a complete assessment of scaffold's deformation behavior. The use of commercially available PLA filament, a fully biocompatible material [43, 44] and low-cost FFF printing solutions has been proven effective in order to manufacture bone replacement scaffolds [1]. Several authors use simple scaffold designs, with single or double-layer configurations, of parallel filaments extruded in a continuous motion [1, 8, 29, 45, 46]. But 3D printing might even be used to produce more complex scaffold geometries, like the gyroid periodic surface, mimicking trabecular biological structures [14].

Scaffolds comprised of parallel filaments printed at three different offset distances were manufactured. Ranging from 571 to 1333 µm, these offset distances allowed for 30 to 70% porosity scaffolds, with pore sizes between 171 and 933 µm in theory. While some authors consider the ideal scaffold characteristics to include high porosity and 200 to 500 µm pores, in order to enhance cell adhesion, proliferation, ECM production and tissue regeneration [2, 17]. Different reports show that other characteristics, like pore surface finish or permeability, enable pores up to 1200 µm to be as effective in bone tissue regeneration [19, 20]. Two different pore designs were produced, one with single-layer aligned filaments (*Ortho*), and other with double-layer staggered filaments (*2xDispl*). Theoretical pore design does not affect scaffold porosity. Printed with previously optimized parameters, both printing temperature and speed influence filament dimensions [23, 24]. Higher temperatures and lower speeds will increase filament width. Both parameters were set according to PLA supplier specifications and previous experiments [41, 47, 48]. SEM morphology analysis showed that scaffold infill percentage affects minimum filament width. For single-layer scaffolds, lower infill percentage (30%) lead to filament stretching during printing. Filament width decreased from 403 µm on crossover points to 299 µm while suspended (Table 2). This finding was already verified by Domingos et al. [29], Yan et al. [49] or Trachtenberg et al. [8], for PCL and PLA scaffolds. While Gleadall et al. [42] considers this feature to be fundamental in order to explain scaffold's mechanical behavior. Higher scaffold infill values (70%) reduced filament stretching, as filament support points are closer together, decreasing the difference between filament maximum (387 µm) and minimum (351 µm) width (Table 2). For double-layer scaffolds, minimum filament width was still found to be proportional to filament offset distance, but the support provided by the first layer, reduced filament stretching to a minimum. The average filament width was not found to be proportional to scaffold infill but is higher for double-layer scaffolds.

According to Domingos et al. [29] and Moroni et al. [50], scaffold pore size, porosity and mechanical performance is highly dependent on filament width. With an overall filament width smaller than the 3D printer nozzle diameter (400 µm), pore areas were consistently higher than the designed values (Fig. 14c). Pore area reached 1.007 mm^2 for the *Ortho-30* scaffold and 0.903 mm^2 for the *2xDispl-30* scaffold, for a design value of 0.870 mm^2. With increasing scaffold infill, the difference between measured and designed pore area increased, reaching a maximum of 55% for the *Ortho-70* scaffold (Table 2). These values reveal the limitations of the FFF technology for manufacturing scaffolds with pores

Table 7 Apparent compressive moduli, E_{num}, for each scaffold, with $E_{fill} = 1903$ MPa

Specimen	E_{exp} (MPa)	E_{num} (MPa)	Error (%)
Ortho-30	239 ± 31	194	− 18.91
Ortho-50	570 ± 19	553	− 2.94
Ortho-70	918 ± 22	1022	11.28
2xDispl-30	89 ± 3	84	− 5.88
2xDispl-50	414 ± 5	432	4.44
2xDispl-70	913 ± 5	1023	12.01

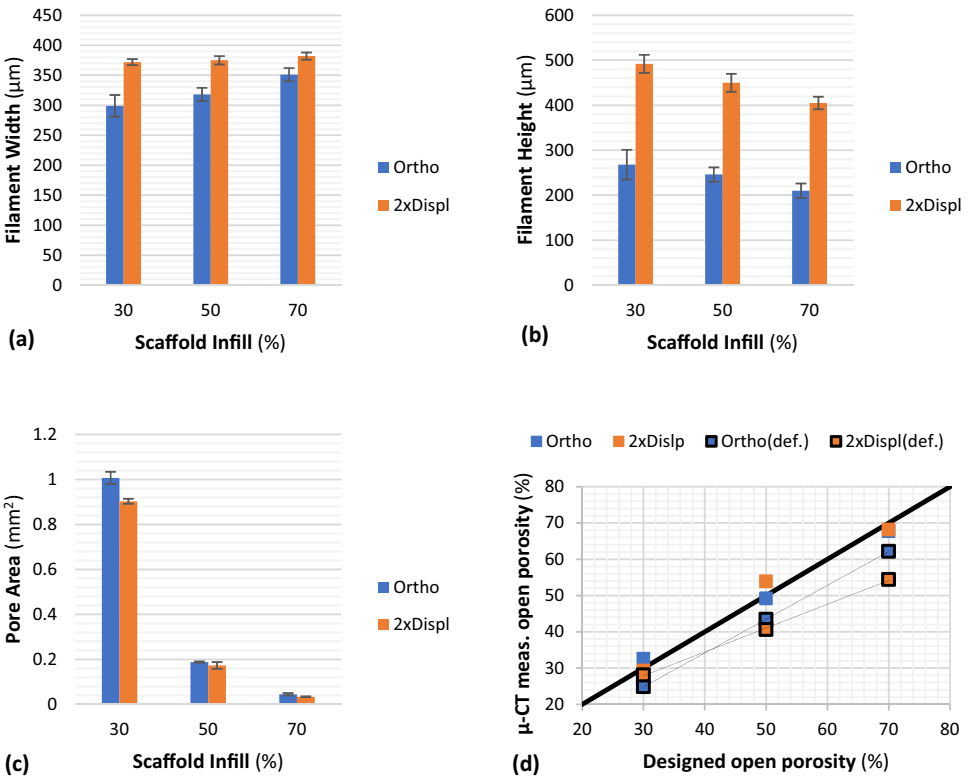

Fig. 14 **a** minimum filament width measured using SEM images, **b** maximum filament height measured using Micro-CT volume analysis, **c** pore area measured using SEM images and **d** scaffold's designed open porosity vs measured by Micro-CT volume analysis for both Ortho and 2xDispl scaffolds

smaller than 171 µm, affecting both scaffold's porosity and mechanical performance. Relationship between filament width (Fig. 14a) and height (Fig. 14b) was consistence with the design amount of material to be extruded per layer. 3D printing process parameters were well optimized. Scaffold porosity was determined using Micro-CT volume analysis [14, 49]. Good correlation was found between designed and measured scaffold density (Fig. 14d). Scaffold's open porosity was also measured and a minimum of 99.9% of interconnected pores was found. FFF 3D printing is therefore a viable tool to manufacture scaffold for bone replacement, as pore interconnectivity is essential for cell migration, oxygenation, nutrient diffusion and waste product removal [51].

Micro-CT analysis also showed that object surface-to-volume ratio decreases with scaffold's infill percentage (Tables 4, 5). As more crossover points are added to the structure, less object surface is available for cell adhesion and growth, within the same object volume. A maximum ratio of 9.38 mm^{-1} was obtained for the *Ortho-30* scaffold. On the other hand, increasing scaffold infill, increases the overall available surface area available for cell adhesion and growth, increasing scaffold surface density. A maximum value of 5.03 mm^{-1} was obtained for the *Ortho-70* scaffold. Overall, both ratios were higher for single-layer scaffolds, as on double-layer scaffolds one filament face is shared between layer, reducing the available surface for cell adhesion and growth.

Under compression, scaffold's behavior (Fig. 7) was similar to polymeric porous media [14, 29, 32, 52]. From the initial linear elastic region, the scaffold's apparent compression modulus was determined. And from the transition between the initial and the second region, occurring around 4–5% strain, the yield stress was also determined. Due to parameter optimization the lowest apparent compressive modulus was obtained for the *Ortho-30* scaffold (239 MPa). This value is higher than the one obtained by Germain et al. [14] in similar conditions. Increasing scaffold infill, increased apparent compressive modulus, due to a higher number of crossover points per square millimeter. On aligned scaffolds these points are responsible for load transmission between layers and scaffold's stiffness [16]. Obtained scaffold apparent compressive modulus increased to 570 MPa for the *Ortho-50* scaffold, a higher value than the ones obtained by Rodrigues et al. [52] (300 MPa) or Corcione et al. [32] (239 MPa) for similar PLA scaffolds, but similar to the one obtained by Rosenzweig et al. [53] (550 MPa). Maximum scaffold apparent compressive modulus, 918 MPa, was obtained for the *Ortho-70* scaffold (Fig. 15b). Several authors have manufactured and tested staggered scaffold configurations, and verified that by staggering consecutive layers, structural bending is introduced, reducing scaffold's apparent compressive modulus [16]. Crossover points, where load is transmitted between layer, are no longer shared. Each filament now acts as a suspended beam with an applied load

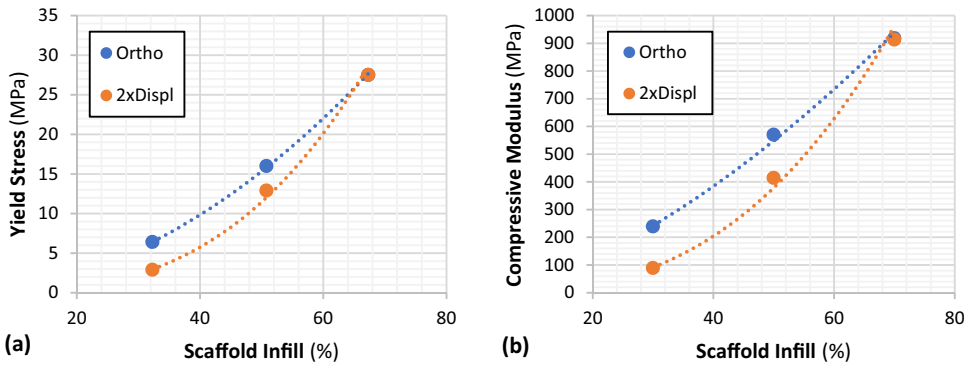

Fig. 15 Scaffold experimentally determined monotonic compression behavior: **a** monotonic yield stress and **b** monotonic apparent compressive modulus, for Ortho and 2xDispl scaffold designs

in the middle section. Scaffold's apparent compressive modulus is expected to decrease around 50 to 70% [1, 46, 54]. *2xDispl-30* scaffold apparent compressive modulus decreased to 89 MPa, a 62% reduction when compared to the *Ortho-30* scaffold. A similar behavior was verified by Serra et al. [46]. *2xDispl-50* scaffold apparent compressive modulus decreased to 414 MPa, a 27% reduction, while almost no decrease was verified for the *2xDispl-70* scaffold (Fig. 15b). Therefore, using higher infill scaffolds improved staggered scaffold's mechanical performance.

When compared with human and bovine trabecular bone, the designed scaffolds meet both the necessary yield stress and apparent compressive modulus. With a wide variety of values available from the literature [55, 56], trabecular bone yield stress may range from 1.92 MPa [57] to 14.22 MPa [58]. According to Taylor [59] testing conditions, preservation methodology and species differences may justify such discrepancies. Determined scaffold's yield stress ranged between 2.9 MPa (*2xDispl-30*) and 27.5 MPa (*Ortho-70* and *2xDisp-70*). With a good correlation found between yield stress and scaffold infill (Fig. 15a), it is possible to tailor scaffold yield stress in order to manufacture specific scaffolds according to application requirements using a power law relationship:

$$Y = a\rho^b \tag{8}$$

where a and b power-law parameters can be determined (Table 8) using scaffold's ρ density.

Trabecular bone apparent compressive modulus is also subject to variation. Skalka et al. [60] determined an average value of 291 MPa, while other authors report a range between 50 and 500 MPa [55, 56]. Once again, designed scaffolds cover this range, and scaffold's infill might be used to tailor specific bone replacement scaffolds (Fig. 15b) [61].

An increase in temperature brings about changes in the state of the amorphous polymer (e.g., PC, GPPS, PMMA, PVC, ABS), and hence, brings changes in the tensile behavior of the polymer. Semi-crystalline polymers follow the mechanical behavior of amorphous polymers at the low temperature. Hence, their ductile–brittle transition temperature is established by the amorphous content of the material. Brittleness is a general term indicating that a polymer absorbs relatively little energy during fracture, i.e., it may simply mean that it breaks easily, while ductility of a material is its ability to deform under load. It is above this transition temperature that polymers become sufficiently ductile that they can exhibit necking. Thus, the more crystalline is the material is, the less sensitive it is to the changes brought by the amorphous content.

Crystalline polymers show high strength & less ductility than the same polymers in the amorphous state at the same temperature. Melt processing to shape polymers may introduce several features which can promote embrittlement, e.g., Development of anisotropy by alignment of molecules or fibrous fillers; inhomogeneity giving a distribution of microstructure throughout the wall thickness of a product or residual stress caused by solidification from the melt during cooling.

Thermal analysis results show different degrees of crystallinity for aligned and staggered scaffolds (Fig. 9c). Both were higher than the crystallinity degree of the original PLA filament before 3D printing. Crystallinity also increased with scaffold infill. By increasing infill value, the offset distance between filament decreases, increasing the number of

Table 8 Power-law correlation parameters between scaffold density and both yield stress and apparent compressive modulus

Scaffold design	Yield stress			Apparent compressive modulus		
	a	b	r^2	a	b	r^2
Ortho	0.0182	1.7266	0.9992	1.0599	1.5975	0.9976
2xDislp	0.0003	2.6766	0.9953	0.0075	2.7690	0.9958

stretching operation during scaffold manufacture. Increasing scaffold infill also increases the amount of material printed by square millimeter, decreasing filament cooling. This allows for higher chain mobility and alignment, increasing scaffold crystallinity. When printing a double-layer configuration, while the first layer is still stretched during 3D printing, the second layer is fully supported, and minimum stretching will occur. This assumption is in good agreement with the lower filament width variation found in SEM analysis and with the lower material crystallinity degree found on double-layer staggered scaffolds. Figure 8c shows that aligned scaffolds fracture appear to occur in brittle mode, while Fig. 8f shows that staggered scaffold fracture appears to occur in ductile mode. Thermal analysis results confirm that the stronger and less ductile scaffolds correspond to a higher degree of crystallization.

Micro-CT analysis shows that scaffold compression resulted in areas where shear deformation dominates. This is a consequence of high specimen height and internal scaffold defects, leading to buckling. This may be considered an ASTM-D695 standard limitation, as in practice scaffolds are applied as multiple lower profile sections, reinforced with an intramedullary nail or plate. Bending and shear are supported by these components, and scaffold will be mainly subjected to compression loads [62]. Even after 40% compression testing, all remaining pores are fully interconnected, maintaining the necessary environment for cell development and activity. Still, open porosity decreased for all scaffold configurations, reaching a minimum value of 24.85% for the *Ortho-70* scaffold. This is a consequence of macro-pore collapse, due to compression. While pore collapse leads to scaffold stiffness increase, less surface area will be available for cell adhesion and growth, as verified by an object surface-to-volume ratio and object surface density decrease (Tables 4, 5). When analyzing TiO_2 loaded polyurethane scaffolds, Fostad et al. [63] found strong experimental correlation between scaffold's apparent compressive modulus and (a) density, (b) object surface-to-volume ratio and (c) filament width. No experimental correlation was found between scaffold's apparent compressive modulus and pore area. Our research showed evidence of correlation between scaffold's Mechanical properties and both designed and Micro-CT measured scaffold's density ($r > 0.9976$, $p < 0.0309$). Regarding object surface-to-volume ratio, experimental correlation to scaffold's apparent compressive modulus evidence was only found for *Ortho* scaffolds ($r = -0.9998$, $p = 0.0131$) [*2xDispl* scaffolds ($r = -0.9708$, $p = 0.1543$)]. No experimental correlation was found between scaffold's mechanical properties and both filament width and pore area ($p > 0.1$). When tailoring scaffold's performance, one must consider that increasing scaffold's mechanical performance will affect cell migration, adhesion and growth.

Future simulations should also cover scaffold permeability, in order to tailor scaffolds ability to support cell oxygen supply, nutrient diffusion and waste removal [30, 64]. According to the Kozeny–Carman model, porous media permeability may be estimated as:

$$K = C_{k-c}\frac{P^3}{S_O^2} \tag{9}$$

where C_{k-c} is a non-dimensional constant [65]. Liu et al. [30] numerical analysis showed that C_{k-c} is a function of scaffold porosity, decreasing with an increase in porosity in a quadratic fashion. Other authors, like Lipowiecki et al. [66] report a constant value of 0.2 for C_{k-c}. In our case, for both *Ortho* and *2xDispl* scaffolds (Eq. 9) renders a twofold decrease in permeability as scaffold's infill increases from 30 to 50% (0.706×10^{-3}–0.336×10^{-3} mm^{-2}) and a sixfold decrease in permeability as scaffold's infill increases from 30 to 70% (0.706×10^{-3}–0.124×10^{-3} mm^{-2}). Once again, increasing scaffold's mechanical performance will affect scaffold's ability to provide cells with the necessary tissue regeneration conditions.

Through finite element simulation, the filament elasticity properties were estimated from their macroscopic counterparts. Simulations indicate that, the elasticity modulus of the filament is of, approximately, 1903 MPa. This value is lower to the one obtained by Gleadall et al. (2450 MPa) [42], but both are within the expected range for PLA for medical applications [67]. With this Young's modulus, estimates for scaffold's apparent compressive moduli were obtained, with relative errors ranging between − 18.91 and 12.01%. These error values are consistent with other works dealing with FEA simulations of scaffolds [30, 42, 68].

According to the simulation results, for the same infill, aligned scaffolds tend to present a higher stiffness than the staggered ones. The higher stiffness of the aligned scaffolds is a result of load transmission along crossover points between different filaments, as opposed to the staggered configurations where the loads between slices are transmitted through filament bending [68]. Figure 16 shows the von Mises Stress field on the *Ortho-30* scaffold, indicating the filaments, outside of the crossover points, only present residual stresses, while the crossover points themselves act as load bearing as observed by Gleadall et al. [42] and by Eshraghi and Das [68]. The results for the staggered filament scaffolds are also consistent with other results in the literature where loads are transmitted between layers through filament bending [16, 46]. This bending behavior can be observed in Fig. 17 where higher stresses occur in regions connecting parallel filaments diagonally along perpendicular filaments.

In this paper, scaffold's apparent compressive moduli were estimated through the computation of the resulting reaction loads over a uniform strain field applied at the top and bottom surfaces. Future works should consider different

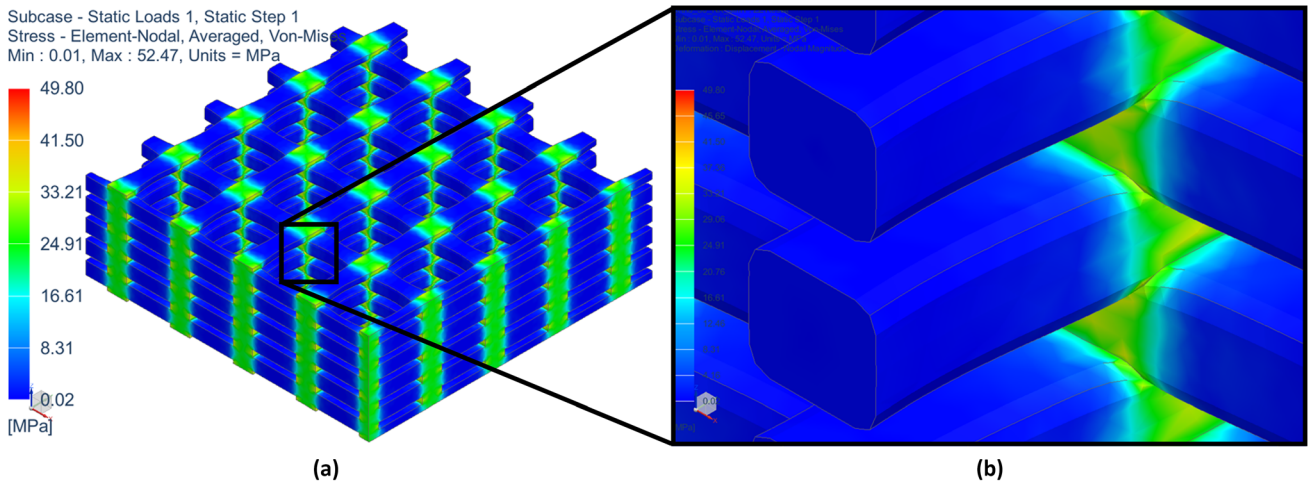

Fig. 16 von Mises Stress field for the Ortho-30 scaffold showing: **a** filament residual stress level and **b** crossover point acting as load bearing

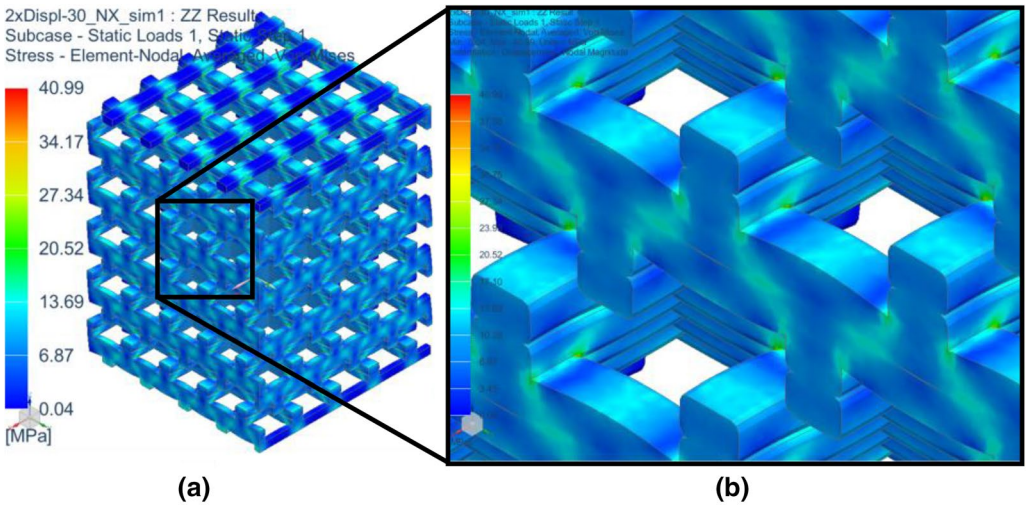

Fig. 17 von Mises Stress field for the 2xDispl-30 scaffold showing: **a** filament bending and **b** higher stress level in regions connecting parallel staggered filaments

approaches for the correlation between microscopic and macroscopic properties such as numerical homogenization. Numerical homogenization is considered one of the most efficient ways to determine the macroscopic properties of non-homogenous materials on the microscopic scale, such as composites or scaffolds [69–71].

Conclusions

This paper presented a complete methodology that combines both experimental and numerical approaches to enhance scaffolding for BTE knowledge. It is possible to tailor scaffold behavior using different infill percentages. By increasing this design parameter, pore size decrease from 933 to 171 µm, while mechanical performance increased to a max. 27.5 MPa yield stress and 918 MPa apparent compressive modulus. Object surface-to-volume ratio decreased with scaffold's infill percentage, while object surface density increased with scaffold's infill percentage, affecting scaffold's permeability. Therefore, as more area becomes available for cell adhesion and growth, permeability will decrease, limiting scaffold ability to provide the necessary conditions for cell proliferation. This shows that while pore size is an important feature, other factors may also improve scaffold behavior. Staggered scaffolds may provide better vertical cell support, but their mechanical properties values decreased up to 62%, due to structural bending. Scaffold infill percentage also affected material crystallinity degree. Increasing scaffold infill percentage, increases the number

of stretching operations and crystallinity degree, leading to filament brittle fracture. It is recommended to print scaffolds using a double-layer configuration, as the first layer will provide additional support, reducing stretching and crystallinity.

Micro-CT volume reconstruction provided the dimensional analysis to create an accurate parametric numerical model for FEM. The model considers both the stretching effect between crossover points, that reduces filament width, and the filament widening effect over crossover points, due to material interference. As infill percentage increased from 30 to 50% on single-layer orthogonal scaffolds, experimental results showed an apparent compressive modulus 2.4-fold increase. The developed model predicted this increase to be 2.9-fold. Between aligned and staggered configurations, the model predicted up to 57% decrease in mechanical properties. This show a good correlation between experimental and numerical results, allowing the model to be used to validate future scaffold designs before manufacturing.

Acknowledgements This work was supported by FCT, through IDMEC under LAETA (project UIDB/50022/2020), CeFEMA (UID/CTM/04540/2019) and CERENA (UIDB/04028/2020). IPFN activities also received financial support from FCT through Projects UIDB/50010/2020 and UIDP/50010/2020.

Author contributions RB, MP, AM, and DR were involved in conceptualization. RB, MP, DR, VI, and MG were involved in methodology. RB, DR, and MG were involved in formal analysis and writing—original draft. RB, MP, AM, DR, VI, and MG were involved in investigation and resources. RB and DR were involved in software. RB and AM were involved in visualization. RB was responsible for supervision. AM was involved in data curation. MP, VI and MG were involved in writing—review and editing. VI and MG were involved in validation.

Compliance with ethical standards

Conflict of interest The authors declare that there is no conflict of interest.

Ethical approval This study does not contain any studies with human or animal subjects performed by any of the authors.

References

1. Gregor A, Filová E, Novák M et al (2017) Designing of PLA scaffolds for bone tissue replacement fabricated by ordinary commercial 3D printer. J Biol Eng 11:1–21. https://doi.org/10.1186/s13036-017-0074-3
2. Roseti L, Parisi V, Petretta M et al (2017) Scaffolds for bone tissue engineering: state of the art and new perspectives. Mater Sci Eng C 78:1246–1262. https://doi.org/10.1016/j.msec.2017.05.017
3. Sin D, Miao X, Liu G et al (2010) Polyurethane (PU) scaffolds prepared by solvent casting/particulate leaching (SCPL) combined with centrifugation. Mater Sci Eng C 30:78–85. https://doi.org/10.1016/j.msec.2009.09.002
4. Thadavirul N, Pavasant P, Supaphol P (2014) Development of polycaprolactone porous scaffolds by combining solvent casting, particulate leaching, and polymer leaching techniques for bone tissue engineering. J Biomed Mater Res Part A 102:3379–3392. https://doi.org/10.1002/jbm.a.35010
5. Intranuovo F, Gristina R, Brun F et al (2014) Plasma modification of PCL porous scaffolds fabricated by solvent-casting/particulate-leaching for tissue engineering. Plasma Process Polym 11:184–195. https://doi.org/10.1002/ppap.201300149
6. Tuzlakoglu K, Bolgen N, Salgado AJ et al (2005) Nano- and micro-fiber combined scaffolds: a new architecture for bone tissue engineering. J Mater Sci Mater Med 16:1099–1104. https://doi.org/10.1007/s10856-005-4713-8
7. Thomson RC, Wake MC, Yaszemski MJ, Mikos AG (1995) Biodegradable polymer scaffolds to regenerate organs. Adv Polym Sci 122:245–274
8. Trachtenberg JE, Mountziaris PM, Miller JS et al (2014) Open-source three-dimensional printing of biodegradable polymer scaffolds for tissue engineering. J Biomed Mater Res Part A 102:4326–4335. https://doi.org/10.1002/jbm.a.35108
9. Nam YS, Park TG (1999) Porous biodegradable polymeric scaffolds prepared by thermally induced phase separation. J Biomed Mater Res 47:8–17. https://doi.org/10.1002/(SICI)1097-4636(199910)47:1%3c8::AID-JBM2%3e3.0.CO;2-L
10. Do KH, Bae EH, Kwon IC et al (2004) Effect of PEG–PLLA diblock copolymer on macroporous PLLA scaffolds by thermally induced phase separation. Biomaterials 25:2319–2329. https://doi.org/10.1016/j.biomaterials.2003.09.011
11. Rowlands AS, Lim SA, Martin D, Cooper-White JJ (2007) Polyurethane/poly(lactic-co-glycolic) acid composite scaffolds fabricated by thermally induced phase separation. Biomaterials 28:2109–2121. https://doi.org/10.1016/j.biomaterials.2006.12.032
12. Malmström J, Adolfsson E, Emanuelsson L, Thomsen P (2008) Bone ingrowth in zirconia and hydroxyapatite scaffolds with identical macroporosity. J Mater Sci Mater Med 19:2983–2992. https://doi.org/10.1007/s10856-007-3045-2
13. Ravi P, Shiakolas PS, Welch TR (2017) Poly-l-lactic acid: pellets to fiber to fused filament fabricated scaffolds, and scaffold weight loss study. Addit Manuf 16:167–176. https://doi.org/10.1016/j.addma.2017.06.002
14. Germain L, Fuentes CA, van Vuure AW et al (2018) 3D-printed biodegradable gyroid scaffolds for tissue engineering applications. Mater Des 151:113–122. https://doi.org/10.1016/j.matdes.2018.04.037
15. Korpela J, Kokkari A, Korhonen H et al (2013) Biodegradable and bioactive porous scaffold structures prepared using fused deposition modeling. J Biomed Mater Res Part B Appl Biomater 101B:610–619. https://doi.org/10.1002/jbm.b.32863
16. Gleadall A, Visscher D, Yang J et al (2018) Review of additive manufactured tissue engineering scaffolds: relationship between geometry and performance. Burn Trauma 6:19. https://doi.org/10.1186/s41038-018-0121-4
17. Zhang L, Yang G, Johnson BN, Jia X (2019) Three-dimensional (3D) printed scaffold and material selection for bone repair. Acta Biomater 84:16–33. https://doi.org/10.1016/j.actbio.2018.11.039
18. Cavo M, Scaglione S (2016) Scaffold microstructure effects on functional and mechanical performance: integration of theoretical and experimental approaches for bone tissue engineering applications. Mater Sci Eng C 68:872–879. https://doi.org/10.1016/j.msec.2016.07.041
19. Hollister S, Lin C, Saito E et al (2005) Engineering craniofacial scaffolds. Orthod Craniofacial Res 8:162–173. https://doi.org/10.1111/j.1601-6343.2005.00329.x

20. Karageorgiou V, Kaplan D (2005) Porosity of 3D biomaterial scaffolds and osteogenesis. Biomaterials 26:5474–5491. https://doi.org/10.1016/j.biomaterials.2005.02.002
21. Moroni L, Poort G, Van Keulen F et al (2006) Dynamic mechanical properties of 3D fiber-deposited PEOT/PBT scaffolds: an experimental and numerical analysis. J Biomed Mater Res Part A 78A:605–614. https://doi.org/10.1002/jbm.a.30716
22. Wieding J, Wolf A, Bader R (2014) Numerical optimization of open-porous bone scaffold structures to match the elastic properties of human cortical bone. J Mech Behav Biomed Mater 37:56–68. https://doi.org/10.1016/j.jmbbm.2014.05.002
23. Baptista R, Guedes M, Pereira MFC et al (2020) On the effect of design and fabrication parameters on mechanical performance of 3D printed PLA scaffolds. Bioprinting 20:e00096. https://doi.org/10.1016/j.bprint.2020.e00096
24. Baptista R, Guedes M (2020) Design and printing parameters effect on PLA fused filament fabrication scaffolds. In: Almeida H, Vasco J (eds) Progress in digital and physical manufacturing. Springer, Cham, pp 131–136
25. Jia S, Yu D, Zhu Y et al (2017) Morphology, crystallization and thermal behaviors of PLA-based composites: wonderful effects of hybrid GO/PEG via dynamic impregnating. Polymers (Basel) 9:528–547
26. Müller AJ, Ávila M, Saenz G, Salazar J (2015) Crystallization of PLA-based Materials. In: Jiménez A, Peltzer M, Ruseckaite R (eds) Poly(lactic acid) science and technology: processing, properties, additives and applications. The Royal Society of Chemistry, London, pp 66–98
27. Gregorova A (2013) Application of differential scanning calorimetry to the characterization of biopolymers. In: Elkordy AA (ed) Applications of calorimetry in a wide context—differential scanning calorimetry, isothermal titration calorimetry and microcalorimetry. InTech, Rijeka, pp 1–20
28. Fischer EW, Sterzel HJ, Wegner G (1973) Investigation of the structure of solution grown crystals of lactide copolymers by means of chemical reactions. Kolloid-Z und Zeitschrift für Polym 251:980–990. https://doi.org/10.1007/BF01498927
29. Domingos M, Chiellini F, Gloria A et al (2012) Effect of process parameters on the morphological and mechanical properties of 3D bioextruded poly(ε-caprolactone) scaffolds. Rapid Prototyp J 18:56–67. https://doi.org/10.1108/13552541211193502
30. Liu H, Ahlinder A, Yassin MA et al (2020) Computational and experimental characterization of 3D-printed PCL structures toward the design of soft biological tissue scaffolds. Mater Des 188:108488. https://doi.org/10.1016/j.matdes.2020.108488
31. Vikingsson L, Gómez-Tejedor JA, Gallego Ferrer G, Gómez Ribelles JL (2015) An experimental fatigue study of a porous scaffold for the regeneration of articular cartilage. J Biomech 48:1310–1317. https://doi.org/10.1016/j.jbiomech.2015.02.013
32. Esposito Corcione C, Gervaso F, Scalera F et al (2019) Highly loaded hydroxyapatite microsphere/PLA porous scaffolds obtained by fused deposition modelling. Ceram Int 45:2803–2810. https://doi.org/10.1016/j.ceramint.2018.07.297
33. Serra T, Ortiz-Hernandez M, Engel E et al (2014) Relevance of PEG in PLA-based blends for tissue engineering 3D-printed scaffolds. Mater Sci Eng C 38:55–62. https://doi.org/10.1016/j.msec.2014.01.003
34. Hoque ME, Hutmacher DW, Feng W et al (2005) Fabrication using a rapid prototyping system and in vitro characterization of PEG-PCL-PLA scaffolds for tissue engineering. J Biomater Sci Polym Ed 16:1595–1610. https://doi.org/10.1163/156856205774576709
35. Todo M, Kuraoka H, Kim J et al (2008) Deformation behavior and mechanism of porous PLLA under compression. J Mater Sci 43:5644–5646
36. Baptista R, Guedes M (2021) Morphological and mechanical characterization of 3D printed PLA scaffolds with controlled porosity for trabecular bone tissue replacement. Mater Sci Eng C 118:111528. https://doi.org/10.1016/j.msec.2020.111528
37. Burg K (2014) Poly(α-ester)s. In: Natural and synthetic biomedical polymers. Elsevier, pp 115–121
38. Kister G, Cassanas G, Vert M (1998) Effects of morphology, conformation and configuration on the IR and Raman spectra of various poly(lactic acid)s. Polymer (Guildf) 39:267–273. https://doi.org/10.1016/S0032-3861(97)00229-2
39. Ross G, Ross S, Tighe BJ (2017) Bioplastics: new routes, new products. In: Brydson's plastics materials. Butterworth-Heinemann, pp 631–652
40. Valainis D, Dondl P, Foehr P et al (2019) Integrated additive design and manufacturing approach for the bioengineering of bone scaffolds for favorable mechanical and biological properties. Biomed Mater 14:065002. https://doi.org/10.1088/1748-605X/ab38c6
41. Senatov FS, Niaza KV, Stepashkin AA, Kaloshkin SD (2016) Low-cycle fatigue behavior of 3d-printed PLA-based porous scaffolds. Compos Part B Eng 97:193–200. https://doi.org/10.1016/j.compositesb.2016.04.067
42. Gleadall A, Ashcroft I, Segal J (2018) VOLCO: a predictive model for 3D printed microarchitecture. Addit Manuf 21:605–618. https://doi.org/10.1016/j.addma.2018.04.004
43. Marei NH, El-Sherbiny IM, Lotfy A et al (2016) Mesenchymal stem cells growth and proliferation enhancement using PLA vs PCL based nanofibrous scaffolds. Int J Biol Macromol 93:9–19. https://doi.org/10.1016/j.ijbiomac.2016.08.053
44. Derakhshanfar S, Mbeleck R, Xu K et al (2018) 3D bioprinting for biomedical devices and tissue engineering: a review of recent trends and advances. Bioact Mater 3:144–156. https://doi.org/10.1016/j.bioactmat.2017.11.008
45. Zein I, Hutmacher DW, Tan KC, Teoh SH (2002) Fused deposition modeling of novel scaffold architectures for tissue engineering applications. Biomaterials 23:1169–1185. https://doi.org/10.1016/S0142-9612(01)00232-0
46. Serra T, Planell JA, Navarro M (2013) High-resolution PLA-based composite scaffolds via 3-D printing technology. Acta Biomater 9:5521–5530. https://doi.org/10.1016/j.actbio.2012.10.041
47. Grémare A, Guduric V, Bareille R et al (2018) Characterization of printed PLA scaffolds for bone tissue engineering. J Biomed Mater Res Part A 106:887–894. https://doi.org/10.1002/jbm.a.36289
48. Choi WJ, Hwang KS, Kwon HJ et al (2020) Rapid development of dual porous poly(lactic acid) foam using fused deposition modeling (FDM) 3D printing for medical scaffold application. Mater Sci Eng C 110:110693. https://doi.org/10.1016/j.msec.2020.110693
49. Yan Y, Chen H, Zhang H et al (2019) Vascularized 3D printed scaffolds for promoting bone regeneration. Biomaterials 190–191:97–110. https://doi.org/10.1016/j.biomaterials.2018.10.033
50. Moroni L, De Wijn JR, Van Blitterswijk CA (2006) 3D fiber-deposited scaffolds for tissue engineering: influence of pores geometry and architecture on dynamic mechanical properties. Biomaterials 27:974–985. https://doi.org/10.1016/j.biomaterials.2005.07.023
51. Park S, Kim G, Jeon YC et al (2009) 3D polycaprolactone scaffolds with controlled pore structure using a rapid prototyping system. J Mater Sci Mater Med 20:229–234. https://doi.org/10.1007/s10856-008-3573-4
52. Rodrigues N, Benning M, Ferreira AM et al (2016) Manufacture and characterisation of porous PLA scaffolds. In: Procedia CIRP. pp 33–38

53. Rosenzweig DH, Carelli E, Steffen T et al (2015) 3D-printed ABS and PLA scaffolds for cartilage and nucleus pulposustissue regeneration. Int J Mol Sci 16:15118–15135. https://doi.org/10.3390/ijms160715118
54. Szojka A, Lalh K, Andrews SHJ et al (2017) Biomimetic 3D printed scaffolds for meniscus tissue engineering. Bioprinting 8:1–7. https://doi.org/10.1016/j.bprint.2017.08.001
55. Wu D, Isaksson P, Ferguson SJ, Persson C (2018) Young's modulus of trabecular bone at the tissue level: a review. Acta Biomater 78:1–12. https://doi.org/10.1016/j.actbio.2018.08.001
56. Li S, Zahedi A, Silberschmidt V (2018) Numerical simulation of bone cutting. In: Numerical methods and advanced simulation in biomechanics and biological processes. Elsevier, pp 187–201
57. Kopperdahl DL, Keaveny TM (1998) Yield strain behavior of trabecular bone. J Biomech 31:601–608. https://doi.org/10.1016/S0021-9290(98)00057-8
58. Fatihhi SJ, Rabiatul AAR, Harun MN et al (2016) Effect of torsional loading on compressive fatigue behaviour of trabecular bone. J Mech Behav Biomed Mater 54:21–32. https://doi.org/10.1016/j.jmbbm.2015.09.006
59. Taylor D (2000) Scaling effects in the fatigue strength of bones from different animals. J Theor Biol 206:299–306. https://doi.org/10.1006/jtbi.2000.2125
60. Skalka P, Slámečka K, Montufar EB, Čelko L (2019) Estimation of the effective elastic constants of bone scaffolds fabricated by direct ink writing. J Eur Ceram Soc 39:1586–1594. https://doi.org/10.1016/j.jeurceramsoc.2018.12.024
61. Provaggi E, Capelli C, Rahmani B et al (2019) 3D printing assisted finite element analysis for optimising the manufacturing parameters of a lumbar fusion cage. Mater Des 163:107540. https://doi.org/10.1016/j.matdes.2018.107540
62. Koc B, Acar AA, Weightman A et al (2019) Biomanufacturing of customized modular scaffolds for critical bone defects. CIRP Ann 68:209–212. https://doi.org/10.1016/j.cirp.2019.04.106
63. Fostad G, Hafell B, Førde A et al (2009) Loadable TiO2 scaffolds—a correlation study between processing parameters, micro CT analysis and mechanical strength. J Eur Ceram Soc 29:2773–2781. https://doi.org/10.1016/j.jeurceramsoc.2009.03.017
64. Liu F, Mao Z, Zhang P et al (2018) Functionally graded porous scaffolds in multiple patterns: new design method, physical and mechanical properties. Mater Des 160:849–860. https://doi.org/10.1016/j.matdes.2018.09.053
65. Egan PF, Gonella VC, Engensperger M et al (2017) Computationally designed lattices with tuned properties for tissue engineering using 3D printing. PLoS ONE 12:1–20. https://doi.org/10.1371/journal.pone.0182902
66. Lipowiecki M, Ryvolová M, Töttösi Á et al (2014) Permeability of rapid prototyped artificial bone scaffold structures. J Biomed Mater Res Part A 102:4127–4135. https://doi.org/10.1002/jbm.a.35084
67. Bergström JS, Hayman D (2016) An overview of mechanical properties and material modeling of polylactide (PLA) for medical applications. Ann Biomed Eng 44:330–340. https://doi.org/10.1007/s10439-015-1455-8
68. Eshraghi S, Das S (2012) Micromechanical finite-element modeling and experimental characterization of the compressive mechanical properties of polycaprolactone–hydroxyapatite composite scaffolds prepared by selective laser sintering for bone tissue engineering. Acta Biomater 8:3138–3143. https://doi.org/10.1016/j.actbio.2012.04.022
69. Andreassen E, Andreasen CS (2014) How to determine composite material properties using numerical homogenization. Comput Mater Sci 83:488–495. https://doi.org/10.1016/j.commatsci.2013.09.006
70. Duan S, Xi L, Wen W, Fang D (2020) Mechanical performance of topology-optimized 3D lattice materials manufactured via selective laser sintering. Compos Struct 238:111985. https://doi.org/10.1016/j.compstruct.2020.111985
71. Dutra TA, Ferreira RTL, Resende HB et al (2020) A complete implementation methodology for asymptotic homogenization using a finite element commercial software: preprocessing and postprocessing. Compos Struct 245:112305. https://doi.org/10.1016/j.compstruct.2020.112305